The Astronomical Journal, 166:29 (18pp), 2023 July
https://doi.org/10.3847/1538-3881/accddb

Precise Age for the Binary Star System 12 Com in the Coma Berenices Cluster

Rex Lam[1], Eric L. Sandquist[1], Gail H. Schaefer[2], Christopher D. Farrington[2], John D. Monnier[2], Narsireddy Anugu[2], Cyprien Lanthermann[2], Robert Klement[2], Jacob Ennis[3], Benjamin R. Setterholm[4], Tyler Gardner[3,4], Stefan Kraus[5], Claire L. Davies[5], and Jerome A. Orosz[1]
[1] San Diego State University, Department of Astronomy, San Diego, CA 92182 USA
[2] The CHARA Array of Georgia State University, Mount Wilson Observatory, Mount Wilson, CA 13 91023, USA
[3] University of Michigan, Deparment of Astronomy, Ann Arbor, MI 48109, USA
[4] Astronomy Department, University of Michigan, Ann Arbor, MI 48109, USA
[5] Astrophysics Group, Department of Physics & Astronomy, University of Exeter, Stocker Road, Exeter, EX4 4QL, UK
Received 2022 December 8; revised 2023 April 8; accepted 2023 April 10; published 2023 June 26

Abstract

We present measurements of the interferometrically resolved binary star system 12 Com and the single giant star 31 Com in the cluster Coma Berenices. 12 Com is a double-lined spectroscopic binary system consisting of a G7 giant and an A3 dwarf at the cluster turnoff. Using an extensive radial velocity data set and interferometric measurements from the Palomar Testbed Interferometer and the Center for High Angular Resolution Astronomy array, we measured masses $M_1 = 2.64 \pm 0.07 M_\odot$ and $M_2 = 2.10 \pm 0.03 M_\odot$. Interferometry also allows us to resolve the giant and measure its size as $R_1 = 9.12 \pm 0.12 \pm 0.01 R_\odot$. With the measured masses and radii, we find an age of $533 \pm 41 \pm 42$ Myr. For comparison, we measure the radius of 31 Com to be $8.36 \pm 0.15\ R_\odot$. Based on the photometry and radius measurements, 12 Com A is likely the most evolved bright star in the cluster, large enough to be in the red giant phase, but too small to have core helium burning. Simultaneous knowledge of 12 Com A's mass and photometry puts strong constraints on convective core overshooting during the main-sequence phase, which in turn reduces systematic uncertainties in the age. Increased precision in measuring this system also improves our knowledge of the progenitor of the cluster white dwarf WD1216+260.

Unified Astronomy Thesaurus concepts: Stellar ages (1581); Interferometric binary stars (806); White dwarf stars (1799); Stellar evolution (1599); Open star clusters (1160); Spectroscopic binary stars (1557)

Supporting material: machine-readable tables

1. Introduction

Stellar ages are among the most difficult quantities to measure as age is not a directly measurable characteristic, making model interpretation a necessity. As models are needed to derive the age, then stellar mass becomes an important characteristic to know. When we can determine the mass of an evolved star, age precision often will dramatically increase because these stars have such short evolution timescales. The accuracy of the age will still depend on whether the models have accurate physics in them, and uncertainties in internal parameters such as chemical composition cause additional systematic uncertainties. In this project, we are analyzing evolved stars in binary systems that are themselves within star clusters, allowing for mass determinations of the stars and age determination for the wider cluster.

The Coma Ber open star cluster is the second closest open cluster to the Sun (after Hyades), and its extent is now resolvable in the radial direction with distances measured by Gaia (Gaia Collaboration et al. 2021). 12 Com is a spectroscopic binary member of Coma Ber, composed of a G7 giant primary star and an A3 dwarf main-sequence star with an angular separation of ∼20 mas that can be resolved interferometrically (Griffin & Griffin 2011). Griffin & Griffin (2011) presented the most comprehensive study on the orbit of 12 Com. However, masses have not been determined for 12 Com. We seek to use improved radial velocities and interferometry to refine the orbit of the binary. Characterization of the giant star primary, as evolved as it is, should provide the most precise age to date for the cluster.

1.1. Literature Ages

So far, all age analyses for Coma Ber have involved isochrone analysis of color–magnitude diagrams (CMDs) for the member stars. One of the oldest attempts at dating Coma Ber comes from Tsvetkov (1989) who used Population I pulsating stars to determine an age of 410 ± 230 Myr. Casewell et al. (2006) used NextGen isochrones (Baraffe et al. 1998) to determine an age of 450 ± 50 Myr. PAdova and TRieste Stellar Evolution Code (PARSEC) isochrones (Bressan et al. 2012) were used by Holmberg et al. (2007) and Singh et al. (2021) to measure ages of 500 ± 100 Myr and 700 ± 100 Myr, respectively.

The large differences in age as well as the large associated uncertainties stem from the inherent limitations of isochrone analysis. Isochrone analysis primarily uses the turnoff point and evolved stars in its determination of age. For Coma Ber, the stars around the turnoff point show significant scatter in CMDs similar to that of Hyades and Praesepe (Brandt & Huang 2015). As such, it is likely that any analysis solely involving isochrone fitting is underestimating the uncertainties in the age determination. In addition, there are only two giant stars (the giant in 12 Com, and 31 Com) in the whole cluster, and to use 12 Com in an analysis, one must be able to measure the characteristics of the two stars separately.

1.2. Distance, Reddening, and Metallicity

Coma Ber is one of the closest clusters to us, which means there are precise parallax measurements of cluster stars. Bailer-Jones et al. (2021) determined distances and probability distributions for individual cluster stars from Gaia Early Data Release 3 (Gaia Collaboration et al. 2021) parallaxes, including accounting for nonzero parallax zero-points. The distance to 12 Com was 86.99 ± 1.19 pc, which is used below.

Reddening analysis for the Coma cluster has been conducted by multiple groups (e.g., Taylor 2006; Singh et al. 2021) by comparing to objects in Praesepe and Hyades. There is agreement that the foreground reddening of Coma Ber is consistent with zero. Taylor (2006) in particular finds an upper bound for the reddening of Coma Ber of $E(B-V) \leqslant 0.0032$.

Metallicity measurements of Coma Ber quoted in the literature vary around solar, and analyses have been conducted using different types of stars. Friel & Boesgaard (1992) report $[\mathrm{Fe/H}] = -0.06 \pm 0.03$ from an analysis of nine F stars, and $[\mathrm{Fe/H}] = -0.04 \pm 0.02$ from 5 G-type stars. Gebran et al. (2008) used 14 F-type stars to determine $[\mathrm{Fe/H}] = +0.07 \pm 0.09$. More recently Souto et al. (2021) found $[\mathrm{Fe/H}] = 0.00 \pm 0.01$, 0.03 ± 0.01, 0.04 ± 0.01, and 0.04 ± 0.03 for three F-type, four G-type, four K-type, and seven M-type stars, respectively.

2. Observations and Data Reduction

2.1. Spectroscopy

2.1.1. Literature Data

Griffin & Griffin (2011) compiled a list of over 300 primary and over 40 secondary star literature radial velocity measurements. The earliest measurements of the primary star belonged to Vinter Hansen (1940) who used the Hartmann Spectrocomparator at Lick Observatory. One additional measurement was made at Mt. Wilson using the coudé spectrograph at the 100 inch telescope (Herbig & Turner 1953); three using the 36 inch refractor at Lick Observatory (Herbig & Turner 1953); two by Parsons (1983) using the Coudé Spectrograph at the 2.1 m Struve telescope at McDonald Observatory; three by Beavers & Eitter (1986) using the radial velocity spectrometer at the Fick Observatory; one by Cannon (1920) using the 15 inch refractor at the Dominion Observatory at Ottawa; and one by Glushkova & Rastorguev (1991) using a correlation spectrograph at the Zeiss-1000 1 m telescope at Mt. Maidanak Observatory. Massarotti et al. (2008) made nine measurements from the Wyeth Reflector at the Oak Ridge Observatory at Harvard.

Griffin & Griffin (2011) supplemented the literature measurements with their own observations using the ELODIE spectrograph at Observatoire de Haute-Provence (OHP), the spectrometer at the 200 inch Palomar telescope, as well as the Plaskett 1.83 m telescope at the Dominion Astrophysical Observatory (DAO; Harper 1934) during almost a 30 yr period from 1981 to 2009. The DAO observations in particular also allowed measurements of the secondary component. Griffin also used independent radial velocities obtained from Abt & Willmarth (1999) using the coudé spectrograph on the Kitt Peak 0.9 m coudé telescope. All of the data obtained and compiled by Griffin & Griffin (2011) were weighted accordingly and added into our analysis below.

2.1.2. Archival Spectra

We analyzed 16 additional spectra from the ELODIE archive (Moultaka et al. 2004), originally taken over a 26 month period at the 1.93 m telescope at OHP (P.I. X. Delfosse). The spectra have a spectral resolution of $R = 42,000$ with a signal-to-noise ratio (S/N) averaging over 200. The spectra covered 4000–6800 Å and were reduced using the ELODIE pipeline. Of these spectra (Spectra 2), one had much lower S/N than the others (∼26), while another (Spectra 16) had strong atmospheric contamination. Neither was used in our subsequent analysis. The primary star dominates the spectra, and its velocities could be measured with no noticeable effect from the secondary star.

We focused on detection and measurement of the secondary star in the spectra in order to expand its radial velocity data set and better constrain the mass of the primary star. While the secondary star is substantially fainter than the primary, its lines can sometimes be distinguished due to a larger rotational broadening ($v_{\mathrm{rot}} \sim 200$ km s^{-1}) and different spectral type (A3).

We attempted to separate the spectra of the primary giant and the secondary main-sequence star in several ways. We began with spectral disentangling (González & Levato 2006) to split the light contributions from the stars. This involves an iterative determination of the average spectra and fitting of broadening functions derived using two different synthetic spectral templates. This did not produce satisfactory results, largely because the luminosity of the primary is so much larger than that of the secondary ($\Delta m > 3$ mag).

Our most successful attempt involved isolating the signal from the secondary star by subtracting a proxy spectrum for the primary star, similar to the method used by Griffin & Griffin (2011). We used an ELODIE spectrum of 31 Vul (Griffin & Griffin 2011), which is very similar to 12 Com A: both are G7 giants around 10–15$R_{\odot}$ (Keenan & McNeil 1989). 31 Vul's spectra were scaled and Doppler shifted appropriately before being subtracted from each 12 Com spectra. We used a modified version of `BF-rvplotter`[6] to calculate broadening functions (Rucinski 1992) from the subtracted spectra, and we fit analytic rotational broadening functions to determine the radial velocity of the secondary star in each. This was done by utilizing the ATLAS synthetic spectral template from Pollux (Palacios et al. 2010) for the secondary star with a $T_{\mathrm{eff}} = 8500$ and $\log g = 3.5$.

We examined two subsets of spectral lines for the fitting of the secondary spectra–the Balmer lines and the Mg II lines around 4481 Å. Thanks to the earlier spectral type of the secondary star, the Balmer lines clearly stand out in the raw spectra, and have a high signal-to-noise ratio. Mg lines were primarily used in velocity measurements by Griffin & Griffin (2011), and although they have a much smaller S/N than the Balmer lines, they are less affected by pressure broadening. We find that velocities measured when including the Balmer lines were systematically offset toward the system velocity compared to those measured with Mg lines alone. This may be related to the additional pressure broadening involved in the Balmer lines. In our analysis below, we use velocities measured in the 4460–4560 Å spectral range, surrounding the Mg II lines. For the 14 usable spectra, the broadening functions and fits are shown in Figure 1. Both the residual signal from the primary and the signal from the secondary can be seen. The secondary star's lines are much more broadened than the

---

[6] https://github.com/mrawls/BF-rvplotter

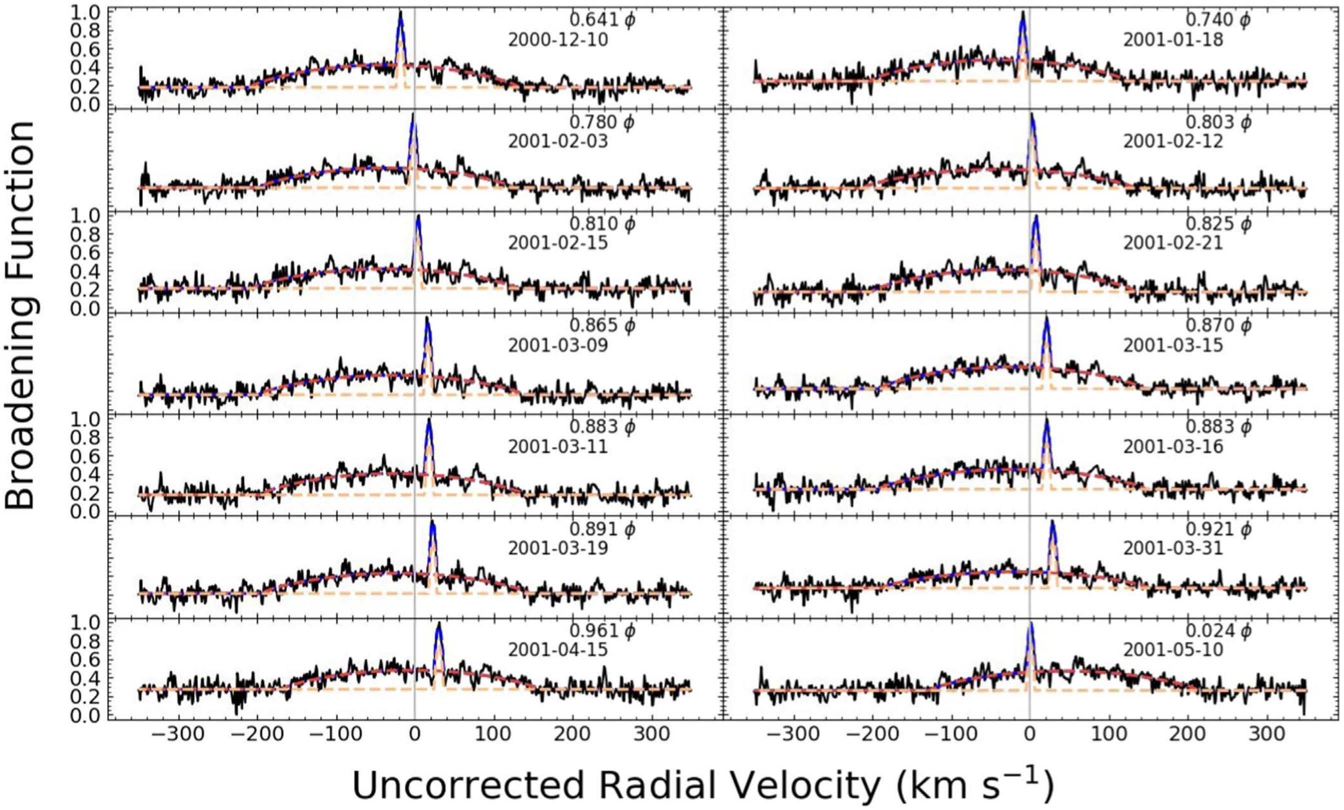

Figure 1. Broadening functions of 14 ELODIE spectra after the primary star's signal was subtracted from the composite spectra. The broadening functions are normalized to the peak value. The blue curve is the fit to the remnant unsubtracted signal from the primary star, while the secondary star's fit is shown in red. Observation dates and associated phase are shown in each panel.

primary's, corresponding to an average rotational speed of 175 km s^{-1}. The ELODIE radial velocities are given in Table 1 and are heliocentrically corrected.

2.2. Data Acquisition

We obtained a small number of archival observations taken over the course of two weeks in 2004 using the Palomar Testbed Interferometer (PTI; Colavita et al. 1999). The PTI observations were extracted from the NASA Exoplanet Science Institute (NExScI) archive. The observations used two-telescope configurations, and so only produced visibility measurements. The wide-band K observations were calibrated against two other stars observed on the same nights, and the visibilities were computed using the software `wbCalib`.[7] These observations, shown in Figure 4, provide our only constraint on the eastern end of the astrometric orbit (see Figure 7).

A larger number of observations were obtained using the Michigan InfraRed Combiner-eXeter (MIRC-X) beam combiner (Anugu et al. 2020) at the Center for High Angular Resolution Astronomy (CHARA) array (10; Brummelaar et al. 2005) at the Mt Wilson Observatory. The MIRC-X instrument interferes the light from up to six telescopes, resulting in visibility measurements on 15 baselines and 20 closure phase triangles. All MIRC-X measurements were taken in the H band using the $R = 50$ (Prism 50), $R = 102$ (Prism 102), or $R = 190$ (Grism 190) spectral modes. Visibilities and closure phases were obtained using the standard MIRC-X pipeline version 1.3.3–1.3.5.[8] The log for the PTI and MIRC-X measurements is given in Table 2, and the measurements of the visibilities and closure phases are given in Tables 3 and 4.

Table 1
New Radial Velocity Measures for 12 Com

mJD[a]	v_A (km s^{-1})	v_B (km s^{-1})
51888.68786	8.90 ± 0.21	−13.66 ± 2.27
51927.66765	14.68 ± 0.21	−19.92 ± 2.32
51943.69036	16.06 ± 0.21	−21.36 ± 1.41
51952.68066	17.41 ± 0.22	−28.66 ± 2.63
51955.64859	17.74 ± 0.21	−28.12 ± 2.01
51961.61818	18.61 ± 0.21	−26.01 ± 2.20
51977.58259	20.82 ± 0.21	−29.73 ± 2.54
51979.51683	21.04 ± 0.21	−24.02 ± 2.26
51984.48075	21.52 ± 0.22	−30.70 ± 2.35
51984.52174	21.52 ± 0.22	−25.84 ± 2.51
51987.53708	21.62 ± 0.21	−28.35 ± 2.44
51999.50986	22.26 ± 0.21	−28.78 ± 1.26
52015.49332	16.06 ± 0.22	−21.81 ± 2.61
52040.43123	−20.40 ± 0.21	18.22 ± 2.59

Note.
[a] mJD = BJD–2400000.

(This table is available in machine-readable form.)

We also obtained MIRC-X observations of the other cluster giant (31 Com) for comparison of radii with 12 Com A. We obtained observations on four nights in 2022 March and April, outlined in Table 2. Although we measured visibilities and closure phases, all of the closure phase measurements were consistent with zero, as expected for a point-symmetric object.

---

[7] https://nexsci.caltech.edu/software/V2calib/wbCalib/index.html

[8] https://gitlab.chara.gsu.edu/lebouquj/mircx_pipeline

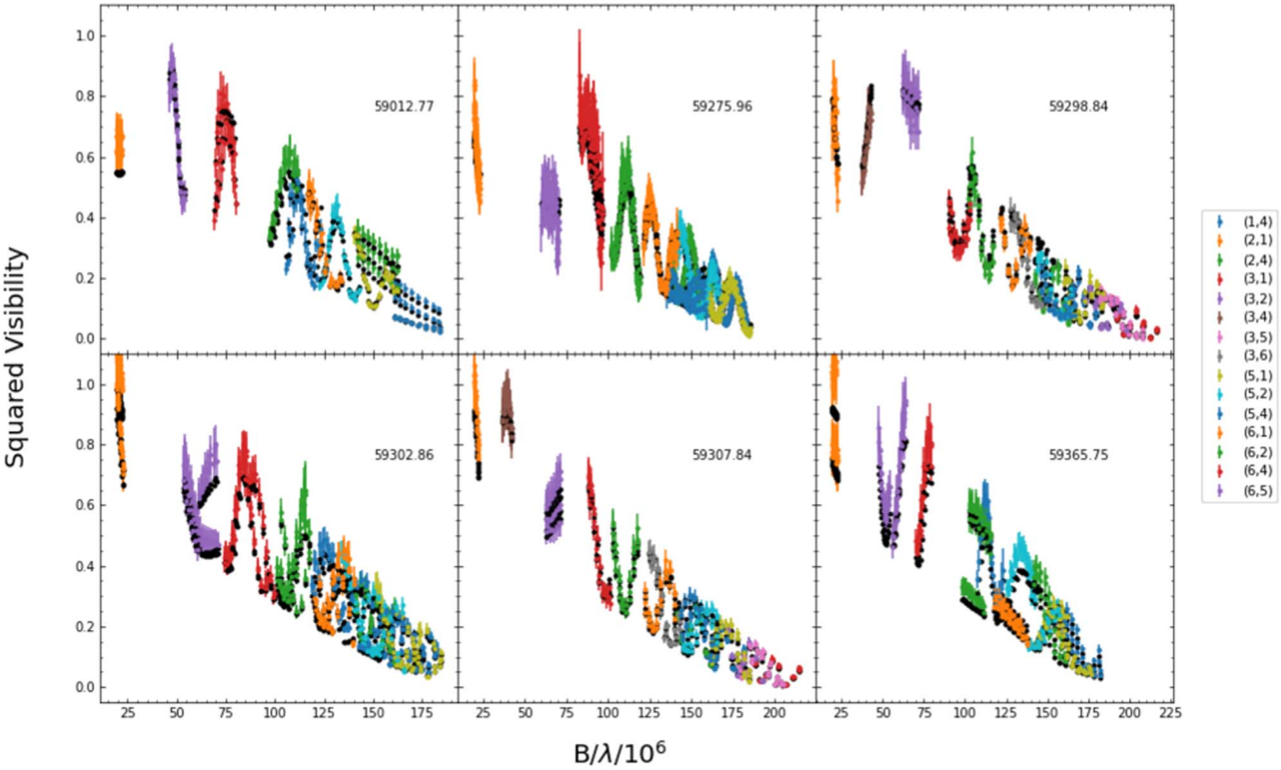

Figure 2. Visibility data and corresponding model fit for the MIRC-X data on 12 Com. The visibilities are split by observation date, where the dates are HJD −2400000. Colors refer to different telescope pairs.

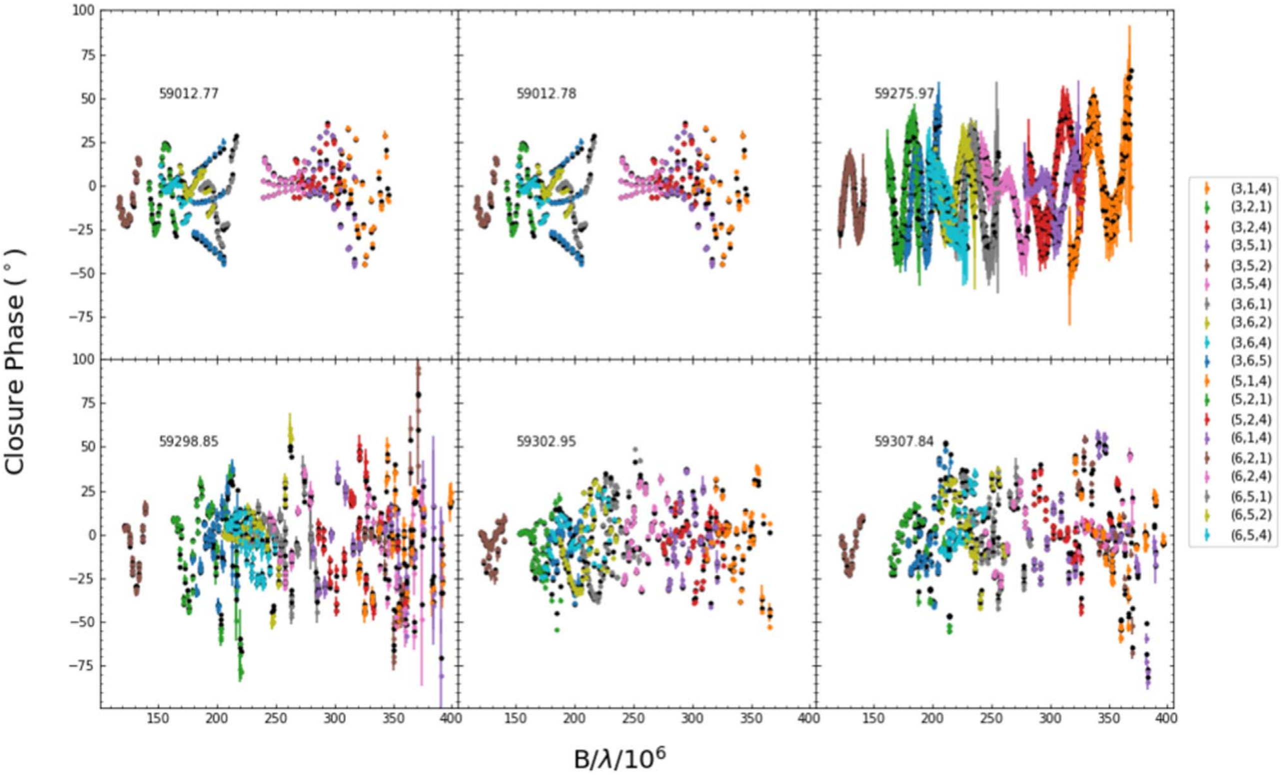

Figure 3. Closure phase data and corresponding model fit for the MIRC-X data on 12 Com. The closure phases are split by observation date, as seen in each panel, where the dates are HJD−2400000. Colors refer to different triplets of telescopes.

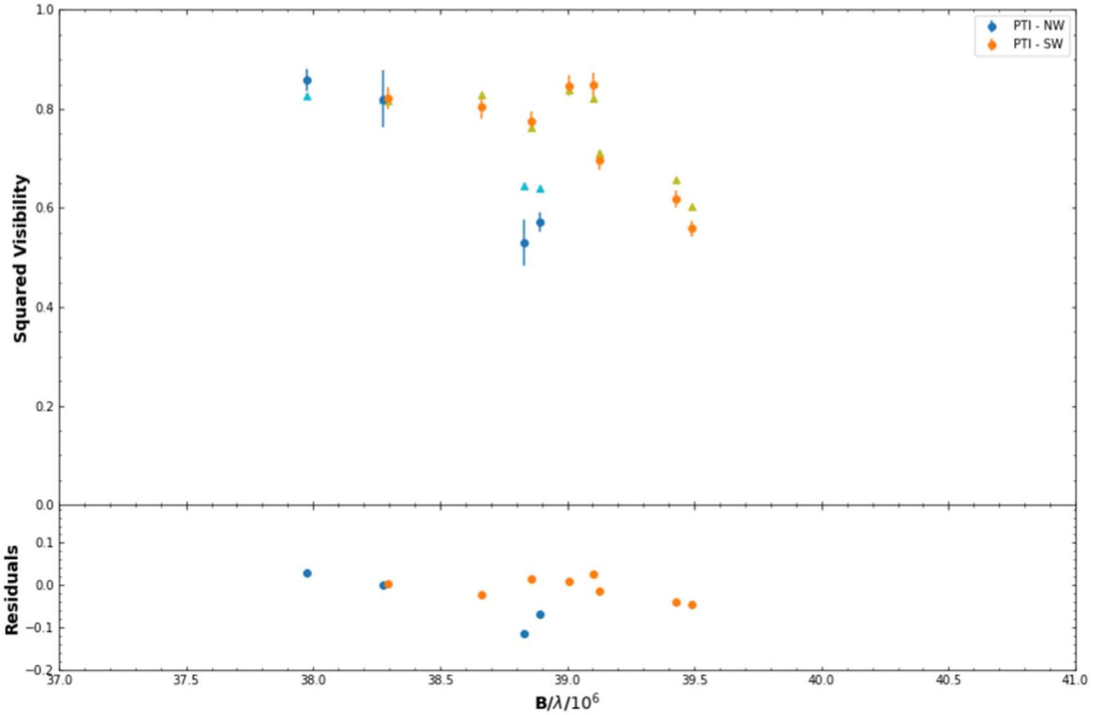

Figure 4. Visibility data and corresponding model fit for the PTI data on 12 Com. All data were taken in a two-week period. Circles and triangles refer to the data and model, respectively. Colors refer to different telescope pairs. The bottom plot shows the residuals between the model and data.

Table 2
Log of Interferometric Observations

Facility	Combiner	HJD Start	UT Date	Spectral Mode	N_{vis}	N_{cp}	Calibrators
				12 Com			
Palomar	PTI (SW)	2453127	5/02/04		2		HD 108471, 108722
Palomar	PTI (SW)	2453132	5/07/04		3		HD 108471, 108722
Palomar	PTI (SW)	2453139	5/14/04		3		HD 108471, 108722
Palomar	PTI (NW)	2453140	5/15/04		2		HD 108471, 108722
Palomar	PTI (NW)	2453142	5/17/04		2		HD 108471, 108722
CHARA	MIRC-X	2459012	6/12/20	Prism 50	320	320	HD 108382
CHARA	MIRC-X	2459275	3/02/21	Grism 190	1398	1400	HD 107966, 108382
CHARA	MIRC-X	2459298	3/25/21	Prism 50	480	640	HD 108382
CHARA	MIRC-X	2459302	3/29/21	Prism 50	640	560	HD 107966, 108382, 113771
CHARA	MIRC-X	2459307	4/03/21	Prism 50	480	640	HD 108382, 113771
CHARA	MIRC-X	2459365	5/31/21	Prism 50	464	396	HD 108382, 113771
				31 Com			
CHARA	MIRC-X	2459655	3/18/22	Prism 50	481	640	HD 113771
CHARA	MIRC-X	2459675	4/06/22	Prism 50 + Prism 102	841	1120	HD 107655, 113771, 116233
CHARA	MIRC-X	2459677	4/08/22	Prism 50	401	480	HD 113771
CHARA	MIRC-X	2459678	4/09/22	Prism 102	961	1280	HD 113771, 116233

Note. Assumed uniform disk calibrator angular diameters: HD 108471: 0.64 mas; HD 108722: 0.48 mas; HD 106661: 0.341 mas; HD 107655: 0.187 mas; HD 107966: 0.358 mas; HD 108382: 0.401 mas; HD 113771: 0.420 mas; HD 116233: 0.188 mas (Bourges et al. 2017).

2.3. Interferometry

We briefly summarize the observable quantities we measured and fit. The visibility amplitude $|\mathcal{V}|$ is defined by how clearly the fringe pattern can be observed. In the case of a uniform disk with angular diameter α, this is:

$$|\mathcal{V}| = \frac{2J_1(\pi B\alpha/\lambda)}{\pi B\alpha/\lambda}. \tag{1}$$

J_1 is the Bessel function of the first kind, and B is the projected baseline of the interferometer based on the star's position in the sky. A binary system can be approximated by two uniform disks, and the observable (squared visibility) is given by:

$$\mathcal{V}_{\text{bin}}^2 = \frac{\mathcal{V}_P^2 + r^2\mathcal{V}_S^2 + 2r|\mathcal{V}_P||\mathcal{V}_S|\cos[2\pi \boldsymbol{B}\cdot \boldsymbol{s}/\lambda]}{(1+r)^2}. \tag{2}$$

Table 3
Visibilities for 12 Com

mJD[a]	$\lambda(\mu\mathrm{m})$	σ_λ	$\mathcal{V}^2$	$\sigma_{\mathcal{V}}$	u (m)	v (m)	Configuration
53127.71391	2.2110	0.4000	0.8799	0.0128	−40.71931	76.02423	SW
53127.76668	2.2104	0.4000	0.5775	0.0153	−53.25317	69.15584	SW
53132.69574	2.2264	0.4000	0.8416	0.0191	−39.41604	76.52089	SW
53132.76592	2.2276	0.4000	0.7214	0.0157	−55.46800	67.23171	SW
53132.81003	2.2232	0.4000	0.8504	0.0203	−60.21185	60.18388	SW
53139.67251	2.2110	0.4000	0.8055	0.0195	−38.20224	76.95870	SW
53139.72202	2.2126	0.4000	0.6394	0.0182	−50.89806	70.85630	SW
53139.77027	2.2100	0.4000	0.8838	0.0248	−58.55339	63.55237	SW
53140.66747	2.2198	0.4000	0.5846	0.0237	−83.51411	−21.87902	NW
53140.72152	2.2162	0.4000	0.8951	0.0227	−77.03038	−33.90183	NW
53142.65695	2.2190	0.4000	0.5209	0.0642	−83.63297	−20.71664	NW
53142.70889	2.2168	0.4000	0.8407	0.0919	−78.42691	−32.37164	NW
59012.76881	1.7083	0.0301	0.9002	0.0757	77.73756	25.37662	E2-S1
59012.76881	1.6819	0.0301	0.8721	0.0734	77.73756	25.37662	E2-S1
59012.76881	1.6516	0.0301	0.8191	0.0691	77.73756	25.37662	E2-S1
59012.76881	1.6206	0.0301	0.7347	0.0621	77.73756	25.37662	E2-S1
59012.76881	1.5890	0.0301	0.6104	0.0519	77.73756	25.37662	E2-S1
59012.76881	1.5568	0.0301	0.5121	0.0438	77.73756	25.37662	E2-S1
59012.76881	1.5240	0.0301	0.4663	0.0400	77.73756	25.37662	E2-S1
59012.76881	1.4983	0.0301	0.4827	0.0414	77.73756	25.37662	E2-S1
59012.76881	1.7083	0.0301	0.3440	0.0300	−112.74443	125.09320	E2-W2

Note. Table 3 is published in its entirety in machine-readable format. A portion is shown here for guidance regarding its form and content.

[a] mJD = HJD–2400000.

(This table is available in its entirety in machine-readable form.)

Table 4
Closure Phases for 12 Com

mJD[a]	λ (μm)	σ_λ	ϕ (°)	σ_ϕ	u_1(m)	v_1(m)	u_2(m)	v_2 (m)	Configuration
59012.76881	1.7083	0.0301	−4.34	1.09	77.73756	25.3766	−190.48198	99.71658	S2-S1-E2
59012.76881	1.6819	0.0301	−7.72	0.86	77.73756	25.3766	−190.48198	99.71658	S2-S1-E2
59012.76881	1.6516	0.0301	−4.65	0.86	77.73756	25.3766	−190.48198	99.71658	S2-S1-E2
59012.76881	1.6206	0.0301	1.80	0.86	77.73756	25.3766	−190.48198	99.71658	S2-S1-E2
59012.76881	1.5890	0.0301	8.47	0.86	77.73756	25.3766	−190.48198	99.71658	S2-S1-E2
59012.76881	1.5568	0.0301	8.42	0.86	77.73756	25.3766	−190.48198	99.71658	S2-S1-E2
59012.76881	1.5240	0.0301	−2.06	0.86	77.73756	25.3766	−190.48198	99.71658	S2-S1-E2
59012.76881	1.4983	0.0301	−11.68	1.27	77.73756	25.3766	−190.48198	99.71658	S2-S1-E2
59012.76881	1.7083	0.0301	1.40	0.86	77.73756	25.3766	−208.69421	127.74149	S2-S1-E1
59012.76881	1.6819	0.0301	2.45	0.86	77.73756	25.3766	−208.69421	127.74149	S2-S1-E1
59012.76881	1.6516	0.0301	−1.21	0.86	77.73756	25.3766	−208.69421	127.74149	S2-S1-E1
59012.76881	1.6206	0.0301	−18.99	0.86	77.73756	25.3766	−208.69421	127.74149	S2-S1-E1
59012.76881	1.5890	0.0301	−33.66	0.92	77.73756	25.3766	−208.69421	127.74149	S2-S1-E1
59012.76881	1.5568	0.0301	−21.27	0.86	77.73756	25.3766	−208.69421	127.74149	S2-S1-E1
59012.76881	1.5240	0.0301	4.12	1.24	77.73756	25.3766	−208.69421	127.74149	S2-S1-E1
59012.76881	1.4983	0.0301	24.77	2.05	77.73756	25.3766	−208.69421	127.74149	S2-S1-E1
59012.76881	1.7083	0.0301	−2.19	0.86	77.73756	25.3766	−125.86196	−135.89354	S2-S1-W2

Note. Table 4 is published in its entirety in machine-readable format. A portion is shown here for guidance regarding its form and content.

[a] mJD = HJD–2400000.

(This table is available in its entirety in machine-readable form.)

Here $\mathcal{V}_P$ and $\mathcal{V}_S$ refer to the complex visibilities of the primary and secondary stars, respectively. The luminosity ratio in the observed wavelength band is given by r. $\boldsymbol{B}$ is the baseline vector for the interferometer, and $\boldsymbol{s}$ is the angular separation vector of the two stars in the sky.

The fringe visibilities are a function of the projected baseline for the interferometer. By utilizing multiple visibilities taken at the same epoch, we can get information about the separation, orientation, and flux ratio of two stars in a binary system. As can be seen for the MIRC-X data in Figure 2, several signatures are present in each epoch. The oscillations as a function of the spatial frequency reveal information about the angular separation of the stars and their orientation on the sky. The amplitude from maximum to minimum of the visibility oscillation gives the binary flux ratio. In addition, the clear downward trend with the spatial frequency is an illustration that the angular diameter of one of the stars is resolved. It is worth noting, however, that systematic uncertainties in the wavelengths of the observations affect the determination of the slope of the visibility curve, which introduce a systematic uncertainty when converting the spatial frequencies to angular scales.

While visibilities can be affected by atmospheric turbulence, we can calculate another observable that is invariable to atmospheric perturbations, namely, the triple product (or more specifically the argument of the triple product) known as the closure phase (Monnier 2007). This quantity measures asymmetry in the light distribution and is well suited to determine the luminosity ratio in any particular band of stars in a binary system. A single point source would have a closure phase of 0°. The closure phases of 12 Com measured with the MIRC-X beam combiner are shown in Figure 3. The maximum and minimum deviations of the closure phases from zero provides the luminosity ratio in the associated wavelength band. As with the visibility amplitudes, the periodicity of the closure phases gives the binary separation and orientation.

2.4. Spectral Energy Distributions

While not the primary focus of this paper, spectral energy distributions (SEDs) were obtained for 12 Com and the other Coma Ber giant star 31 Com from published photometry. More discussion of the data can be found in the Appendix. When we compare the two SEDs (see Figure 5), the binary's SED shows much greater ultraviolet emission than 31 Com. The indications from the analysis below are that 12 Com A is cooler than 31 Com, which emphasizes that this ultraviolet contribution must be coming from a relatively hot companion star.

3. Interferometry and Radial Velocity Modeling

3.1. 12 Com

Before conducting a simultaneous fit to the full interferometric and spectroscopic data set, we first used the Eclipsing Light Curve (Orosz & Hauschildt 2000) code to fit for the systemic radial velocities of the two stars in different spectroscopic data sets. We wish to ensure that the radial velocities are on the same velocity zero-point, as this has some effect on the fitted orbital velocities and stellar masses. Griffin & Griffin (2011) reported that they artificially increased OHP and ESO velocity measurements by 0.8 km s^{-1} in order to keep the Cambridge zero-point velocities (Griffin 1969) for all of the data sets he used. We find that we need to apply an offset of +0.52 km s^{-1} to the ELODIE data set for the primary star to match the Griffin & Griffin (2011) observations, and this is fairly consistent with the Cambridge velocity zero-point. However, the comparison of secondary star data sets indicates that we need to apply an offset of −6.43 km s^{-1}. The secondary star offset is fairly large and may reflect some residual difficulties in measuring the secondary star in the presence of the large primary star signal or measurement differences due to different lines used.

We model the binary's orbit using `interfRVorbit`, which uses a genetic algorithm (Charbonneau 1995) to search for the best binary orbital fit to interferometric measurements (visibilities and closure phases), radial velocities for both stars, and sky position data. Fourteen parameters were fitted: the radial velocity semi-amplitudes of each component (K_p, K_s), eccentricity (e), argument of periastron (ω), orbital period (P), reference time for periastron (t_P), luminosity ratios in the H and K_S bands (r_H, r_K), angular diameter of the primary star (α_P), orbit inclination (i), angular size of the semimajor axis of the binary orbit (a), position angle of the ascending node (Ω), and systemic velocities for both stars (γ_p, γ_s). While we clearly resolve the primary in the interferometric data, the secondary star is not resolved. The angular size of the secondary does have a small effect on the fits, however, and we force the size of the secondary star to be 0.315 mas, based on visible-light interferometric measurements of other Coma Ber stars with similar luminosities and temperatures (Perraut et al. 2020). We initially fitted for the H- and K-band luminosity ratios independently, and the best fits resulted in values that differed by about 25%. However, because the interferometric measurements were taken in wavelength bands well onto the Rayleigh–Jeans portion of the spectral energy distribution, the luminosity ratios are expected to effectively be equal. For that reason, we enforced the equality of the ratios in our fits. Analysis of the interferometric observations indicates that the luminosity ratio L_2/L_1 in the H and K infrared bands is approximately 0.14. Finally, we allowed for different systemic velocities in the fit due to the difference in evolutionary states between the two stars. As discussed in Section 4, one star is a giant, and one is an A-type main-sequence star. Gravitational redshifts (larger for the main-sequence star) and convective blueshifts (probably only important for the giant) can produce differences of order 1 to a few km s^{-1}.

Because different types of observational data can comment on the values of some parameters, it is important to properly weight the distinct data sets. We attempted to do this by empirically determining scalings for the uncertainties that came out of the data reduction process. As much as possible, we fitted subsets of the observed data separately and scaled the uncertainties to return a reduced $\chi^2_\nu \approx 1$. Effectively, this uses observed scatter around the best-fit model as an empirical measure of the uncertainty. For example, we fitted radial velocity data sets from different sources separately to independently determine the scalings for those data.

Overall, 10,000 genetic generations were made to assess uncertainties for each parameter by exploring ranges around the best-fit values. The orbital parameters implied by this fit are given in Table 6, as are the fitting results of Griffin & Griffin (2011) to their radial velocity data set. We obtained uncertainty measurements for the fit parameters by examining parameter ranges at one above the minimum value of χ^2 mark (Avni 1976).

Figure 6 compares the various radial velocity data sets to the fit. With the new set of observations from ELODIE, particularly in the secondary star's radial velocities, we obtain an improved constraint for the velocity amplitude of the secondary star, and thus the mass of the primary.

The best-fitting model of the binary system's astrometric orbit is shown in Figure 7. The positional measurements obtained from CHARA are outlined in Table 5 and were computed using a binary grid search procedure (Schaefer et al. 2016).[9] These position measurements are determined from visibility and closure phase measurements on multiple baselines on single nights and are plotted in black. These positions have associated uncertainties that account for up to 0.06% in the MIRC-X wavelength scales (Gardner et al. 2022). This systematic error source can be estimated to produce an

---

[9] https://www.chara.gsu.edu/analysis-software/binary-grid-search

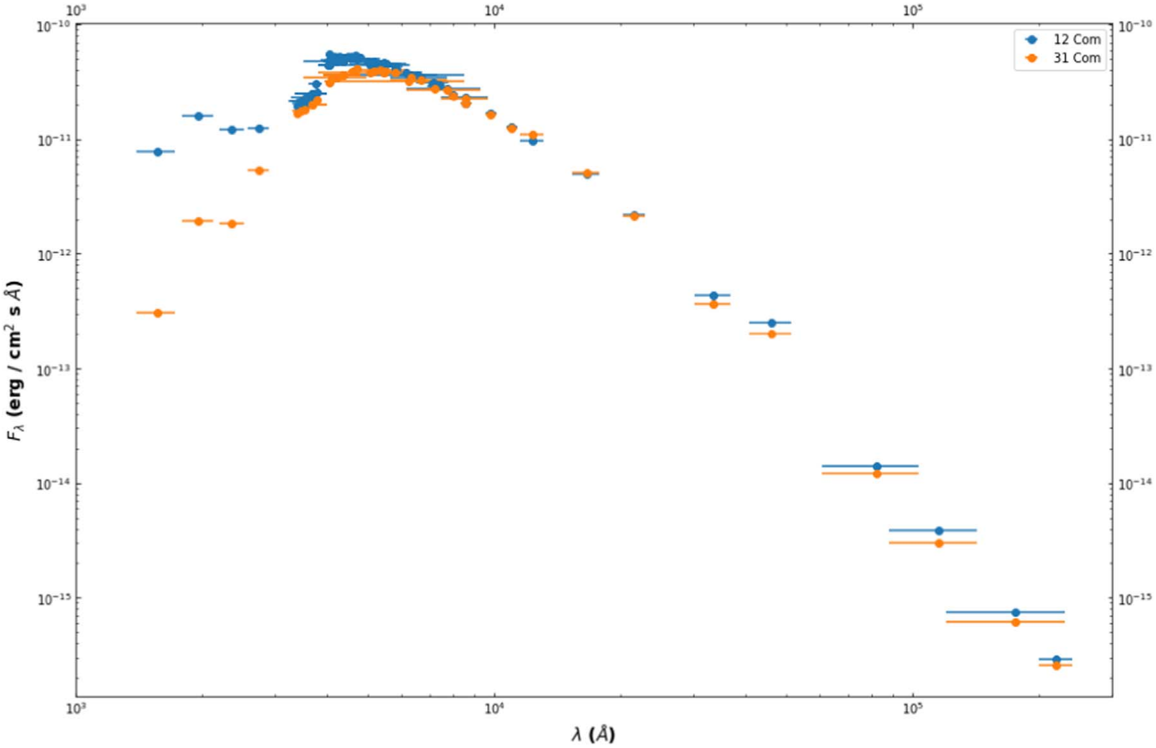

Figure 5. Spectral energy distributions of the single giant star 31 Com and the binary 12 Com, with the photometric passbands for each point indicated with horizontal bars.

uncertainty in distance of 0.05 pc. In the same plot we show the expected position of the secondary star at the time of the PTI observations to give an indication of how these help constrain the orbit size. Because we are constraining the orbit with measurements in two quadrants of the orbit with different instruments, we should be aware of the possibility that the wavelength calibrations might lead to systematics in the orbit determination, but we are not presently able to evaluate them more than this.

We note that the systemic velocity of the secondary star appears to be significantly blueshifted (∼3 km s^{-1}) relative to that of the primary, and that this is in the opposite direction from expectations based on differences in gravitational redshift or convective blueshift for the two stars. Although we do not have an explanation for this at present, what is most important for the majority of our analysis here are the velocity amplitudes, as these are what enter into the mass determinations.

3.2. 31 Com

For the single giant 31 Com, we fitted the interferometric visibilities with a model disk of uniform brightness using two parameters: the angular diameter of the star (α) and the normalization of the visibilities ($\mathcal{V}_0^2$). The second parameter was found to be necessary because the calibrated visibilities consistently reached values above 1 on the smallest baselines. We experimented to check whether our calibration targets (listed in Table 2) may have had incorrect angular diameters, but did not find an explanation for this.

into account We fitted data from each of four nights of observation separately using the `interfRVorbit` code, as shown in Figure 8. There was good consistency between the angular diameters from the nights, and the weighted average value is $\alpha = 0.922 \pm 0.004 \pm 0.005$ mas as shown in Table 7. The quoted uncertainties are statistical (based on the standard deviation of the four measurements) and systematic (assuming 0.06% uncertainty in the MIRC-X wavelength scale). Limb darkening was not included; however, were it to be included, it would likely result in a larger radius measurement and associated uncertainty. A slightly larger radius would not affect our main conclusions.

4. Discussion

While model isochrone analyses have been done many times before for Coma Ber (see Section 1.1), we can now apply new stellar data to the problem. The masses and radii derived from the fit for 12 Com can put strict limits on the age of the cluster. This also provides insight into the fidelity of the internal physics used in different isochrone models, and can identify issues that will allow us to minimize systematic errors. In particular, convective core overshooting is notoriously difficult to model, with different modeling groups utilizing different amounts of overshooting. This directly affects the amount of hydrogen burned on the main sequence, and thus the age.

Data on the brightest stars in the Coma Ber cluster are very helpful to use in connection with the binary star information from 12 Com. We created an initial list of probable members from a Gaia EDR3 sample. Stars with $G < 18$ were considered candidates if positions were within 15° of $(\alpha, \delta) = (186\overset{\circ}{.}38, 25\overset{\circ}{.}42)$, proper motions were within 2.5 mas yr^{-1} of $(\mu_\alpha, \mu_\delta) = (-12.1, -9.0)$ mas yr^{-1}, and parallaxes were within 0.3 mas of 11.64 mas (Gaia Collaboration et al. 2021). We also incorporated stars in the cluster's tidal tails from the more thorough surveys by Tang et al. (2019) and Fürnkranz et al. (2019). When available, we also used radial velocity information from Mermilliod et al. (2008) or Gaia DR2 (Gaia Collaboration et al. 2018) to check membership (using the mean $v_r = 0.21 \pm 0.13$ km s^{-1}; Gaia Collaboration et al.).

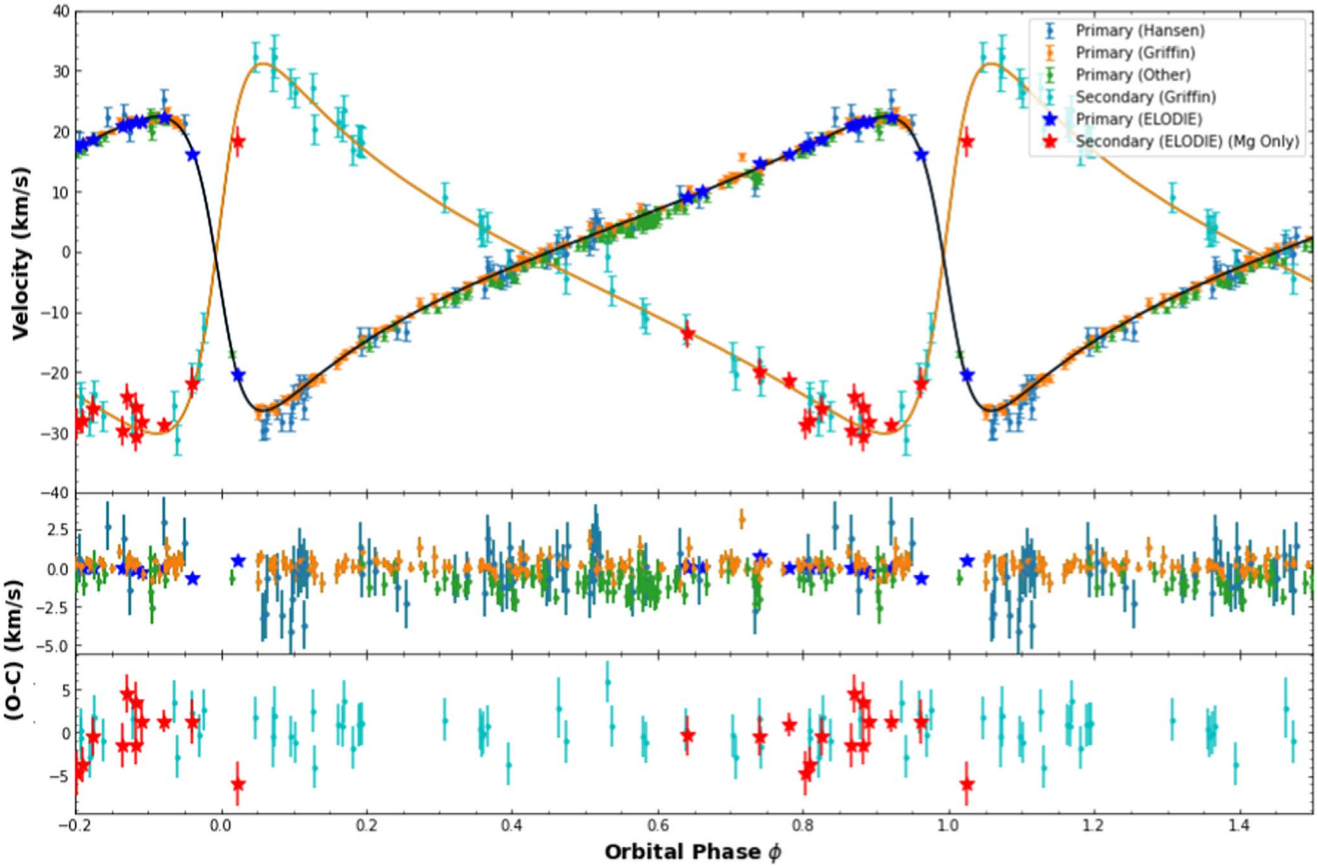

Figure 6. Top: Radial velocity measurements from ELODIE (red and blue stars) and literature data vs. phase, along with the best-fit orbit model. Middle/bottom: Velocity residuals (observed minus computed) for the primary and secondary stars, respectively. Primary star measurements from Griffin & Griffin (2011) between orbital phases of −0.05 and 0.05 were removed due to likely contamination by the secondary star.

The cluster contains only two bright stars that have evolved off the main sequence–one of the stars of 12 Com and 31 Com. 31 Com is a single rapidly rotating variable subgiant in the Hertzsprung gap. Strassmeier et al. (1994) identified major star spots (revealing a rotational period of 6.8 days) and a large rotational velocity ($v_{\rm rot} \sin i = 67 \pm 2$ km s^{-1}). We can also derive the effective temperature $T_{\rm eff} \approx 5700 \pm 40$ K by comparing the SED of 31 Com with synthetic spectra (see Figure 13 and Appendix). The bolometric flux can also be derived from the SED fit combined with the Gaia distance in order to get a luminosity of $63.6 \pm 1.0\, L_\odot$. Pairing this with the effective temperature, we find that 31 Com has a radius of $8.18 \pm 0.13\, R_\odot$. This measurement is in rough agreement with the radius derived from the interferometry ($8.36 \pm 0.15 R_\odot$). Typically, a large scatter around the long baseline end implies asymmetric structures or stellar spots. As such, the lack of scatter in the visibilities of 31 Com in Figure 8 suggests that 31 Com is nearly circular in shape. These data show that 31 Com is clearly smaller in size than 12 Com A, but despite the rapid evolution timescale for these giants, the radii are fairly similar. If an asteroseismic determination of its mass could be accomplished, the star could also provide a strong constraint on the cluster age.

4.1. Mass–radius Isochrones

One of the results of this paper is that interferometric observations have resolved the primary star 12 Com A. Using the angular diameter of the primary with the Gaia distance for 12 Com (86.99 ± 1.19 pc; Bailer-Jones et al. 2021), we find a primary star radius of $9.12 \pm 0.12 \pm 0.01 R_\odot$, where the first and second uncertainties are estimates of the statistical and systematic uncertainties, respectively. The statistical uncertainty includes the contributions from the model fit for the angular diameter as well as the Gaia distance. The systematic uncertainty derives from a 0.06% uncertainty in the MIRC-X interferometer wavelength scale.

This radius tells us that even though the binary's color is bluer than 31 Com, the primary star in the binary is larger than 31 Com, and this is a clue that it is likely to be redder and slightly more evolved. We compare 12 Com A's characteristics with the Modules for Experiments in Stellar Astrophysics (MESA) Isochrones and Stellar Tracks (MIST; Choi et al. 2016) in the mass–radius plane in Figure 9. With the relatively large uncertainty for the mass, the radius constrains the age of the cluster to about 538 ± 38 Myr. The radius measurement does rule out the possibility that the primary star is in the red clump phase, which would require it to be significantly larger, and in fact, constrains the evolutionary phase to near the luminosity minimum at the base of the red giant branch (where there is a small kink in the isochrones).

4.2. Evolutionary States of the Stars

Figure 10 shows theoretical isochrones from the PARSEC (Bressan et al. 2012) and MIST (Choi et al. 2016) databases (shown with solid and dotted lines, respectively) plotted against data for cluster members. This comparison is done with

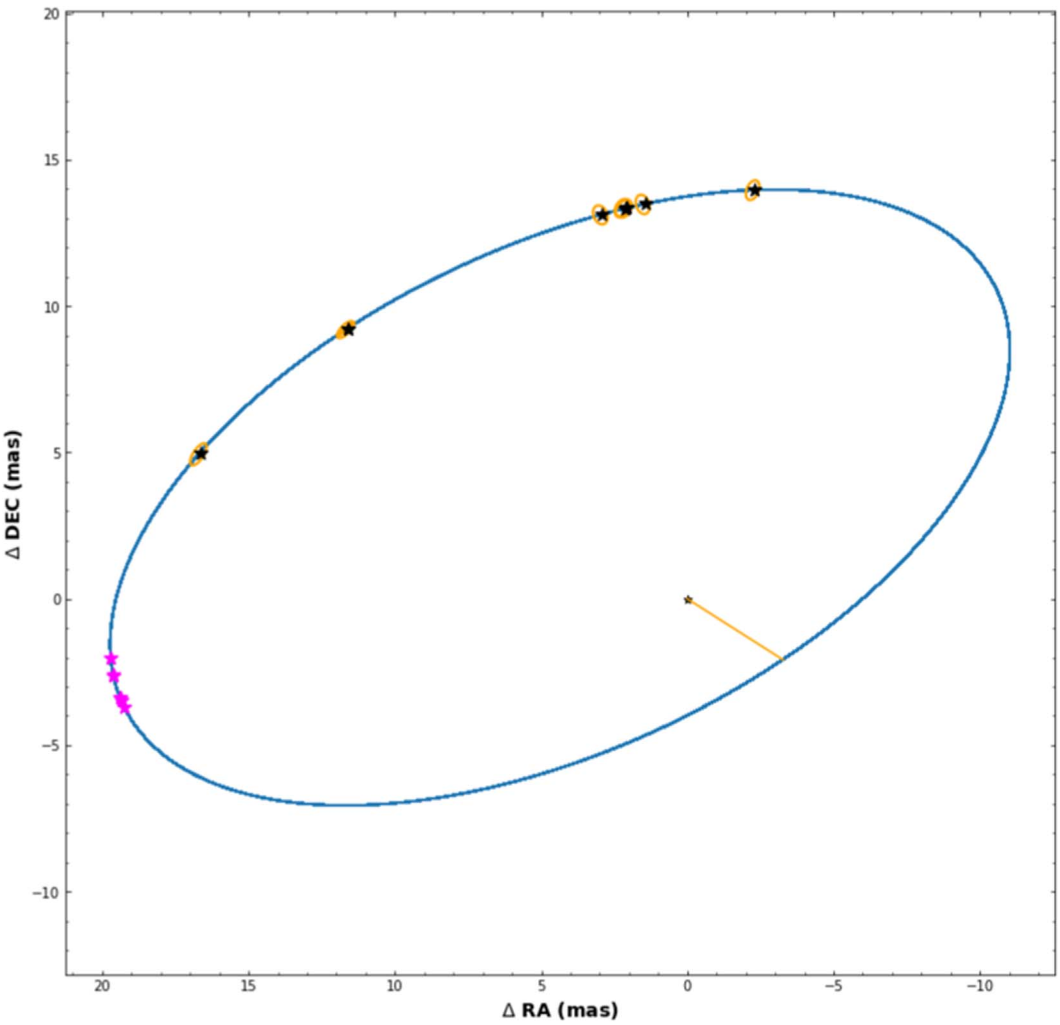

Figure 7. Relative orbit for 12 Com B with respect to 12 Com A, represented by the star at (0,0). The purple and black points show the model-predicted positions of the secondary star at the time of PTI and CHARA observations, respectively. Positions derived from the visibilities are coincident with the model-predicted positions. The orange ellipses show a 10σ uncertainty around the calculated positions. The yellow line connects 12 Com A to the periastron.

PARSEC v1.2 rather than newly introduced 2.0. The latter version uses a smaller maximum core overshooting parameter ($\lambda_{\rm ov,max} = 0.4$ rather than $\lambda_{\rm ov,max} = 0.5$), as well as a diffusive treatment for convective mixing. This results in a hotter and slightly fainter MS phase and a fainter subgiant phase (Nguyen et al. 2022). The comparison of isochrones emphasizes that uncertainty in the amount of convective core overshooting affects the measured age of the cluster by tens of Myr.

As 12 Com is a binary system, the photometry of the stars in the binary must be disentangled for comparisons with evolutionary models. The two components of 12 Com obviously must be dimmer than the binary, and one component must be redder than the binary's overall color. This on its own constrains the evolutionary state of the more evolved star to be a late subgiant, an early red giant, or a red clump star, as shown in Figure 11. With our measurement of the radius above, we can rule out the possibility of it being in the red clump.

The age uncertainty is dominated by the uncertainty in the primary star mass because the evolution timescale for the radius is so short in the giant phase. We can further constrain the age by examining the photometry implied for the secondary. By subtracting the allowed photometry for the primary from that of the binary, the secondary star can be localized to a small region near the cluster turnoff point, as shown in Figure 12. The light red curve shows a large range of potential colors and magnitudes, but only those close to the main sequence should be considered if the star has evolved like a normal single star cluster member. This in turn puts somewhat tighter limits on where 12 Com A can be on its evolution track and also slightly reduces the age range allowed. The predicted positions of 12 Com B in the isochrones for its mass (and $\pm 1\sigma$ uncertainty, shown by the black box) do agree with the limits placed by this procedure.

By assuming that 12 Com B is in the intersection between the MIST isochrones and the thick blue curve in Figure 12 (imposed by the allowed photometric positions of 12 Com A for $M_1 - 1\sigma$), we can further delimit the color–magnitude area that 12 Com A can exist in. This range is shown as the cyan box, and it constrains the age to 533^{+42}_{-38} Myr.

To fit the Gaia CMD of the brightest main-sequence stars in the cluster, we find some need to use MIST or PARSEC isochrones with supersolar metal content. The issue is complicated, however, due to continuing uncertainty as to the precise value of the solar metal content $Z_{\odot}$. MIST isochrones and evolutionary tracks use a protosolar metal content $Z = 0.0142$, consistent with the solar composition study of

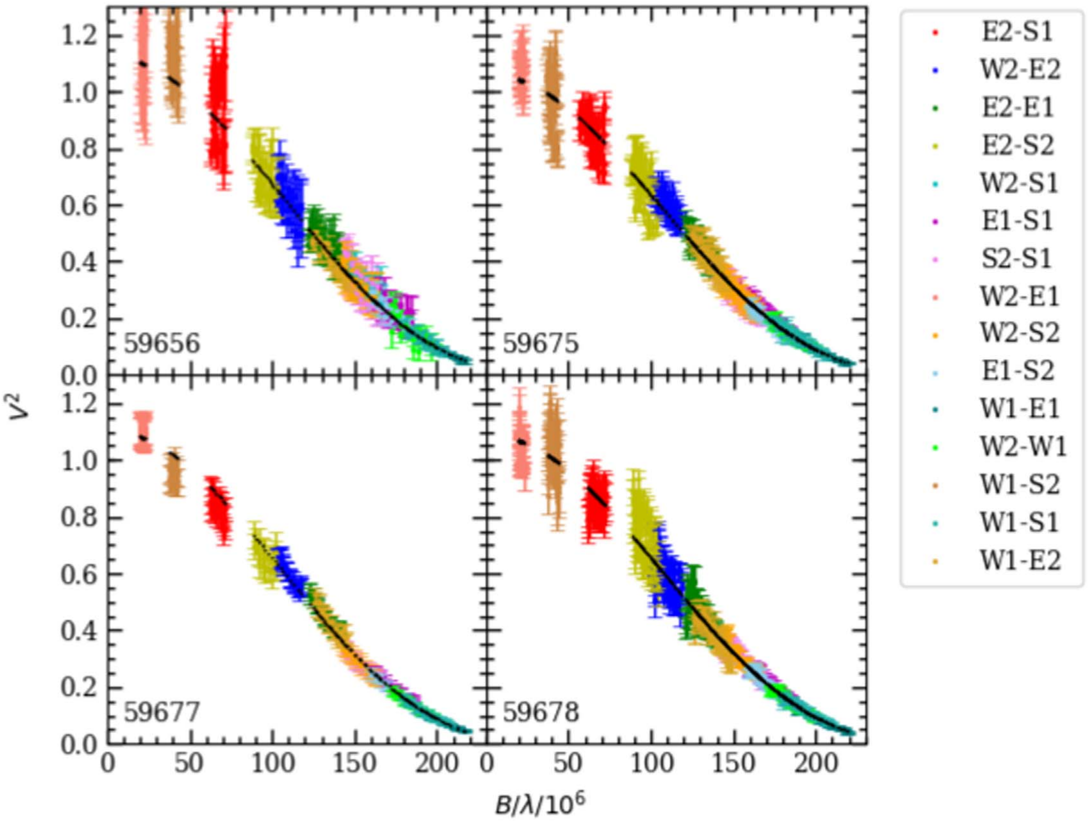

Figure 8. Fits to the interferometric data for the giant 31 Com. The color points show observations with different baselines in the CHARA array, and the black points show the best model fits. Labels give the Julian date of observation–2400000.

Table 5
Fitted Parameters for 12 Com

Parameter	This Study	Griffin & Griffin (2011)
K_P (km s^{-1})	24.399 ± 0.036	24.40 ± 0.06
K_S (km s^{-1})	30.7 ± 0.4	30.6 ± 0.4
P (days)	396.4473 ± 0.0002	396.411 ± 0.009
e	0.599483 ± 0.000026	0.5978 ± 0.014
i (°)	64.8556 ± 0.0011	
ω_1 (°)[a]	100.162 ± 0.001	100.22 ± 0.27
t_P (mJD[b])	46877.148 ± 0.054	46877.57 ± 0.17
$r_H = \frac{L_S}{L_P}(H)$	0.14423 ± 0.00020	
$r_K = \frac{L_S}{L_P}(K)$	0.14423 ± 0.00020	
α_p (mas)	0.97145 ± 0.00046[c]	
a(mas)	20.3358 ± 0.00066[c]	
Ω (°)	118.618 ± 0.004	
γ_P (km s^{-1})	0.51 ± 0.02	0.78 ± 0.04
γ_S (km s^{-1})	−2.75 ± 0.20	
d (pc)	86.78 ± 0.76	
$M_P \sin^3 i$ ($M_\odot$)	1.958 ± 0.054	1.97 ± 0.07
$M_S \sin^3 i$ ($M_\odot$)	1.556 ± 0.023	1.567 ± 0.027
M_P ($M_\odot$)	2.64 ± 0.07	
M_S ($M_\odot$)	2.10 ± 0.03	

Notes.

[a] Based on the longitude of periastron defined from the spectroscopically measured ascending node.

[b] mJD = HJD–2400000.

[c] Uncertainty is purely statistical and does not take the 0.06% in the MIRC-X wavelength scale.

Table 6
Fitted Positions for 12 Com

UT Date	mJD	ρ (mas)	θ (deg)	σ_{maj} (mas)	σ_{min} (mas)	φ (deg)
6/12/2020	59012.273	17.427	73.55	0.087	0.035	56.57
3/02/2021	59275.465	14.140	350.91	0.071	0.041	67.56
3/25/2021	59298.344	13.562	6.50	0.068	0.046	107.48
3/29/2021	59302.367	13.524	9.36	0.068	0.042	41.01
3/29/2021	59302.384	13.521	9.34	0.068	0.052	58.40
3/29/2021	59302.445	13.526	9.46	0.068	0.035	56.71
4/03/2021	59307.343	13.452	12.81	0.067	0.047	111.92
5/31/2021	59365.258	14.877	51.74	0.075	0.011	37.21
5/31/2021	59365.303	14.877	51.81	0.074	0.031	46.65

Note. Column 2: mJD = HJD–2400000. Column 3: angular separation. Column 4: position angle of separation vector measured East of North. Columns 5–7: the major and minor axis size, and orientation angle of the error ellipse.

(This table is available in machine-readable form.)

Asplund et al. (2009). A recent study by Magg et al. (2022) find that solar constraints are much better matched by $Z_\odot = 0.0177$. For the purposes of reproducibility, we will quote the best-fit value used in the isochrones: $Z = 0.0165$. If $Z_\odot$ is the higher Magg et al. value, then Coma Ber would appear to have subsolar metal content ([Fe/H] = −0.03). If the lower Asplund et al. value is correct, then Coma Ber would appear to have supersolar metallicity ([Fe/H] = +0.07). In either case, the metallicity [Fe/H] would be within the range

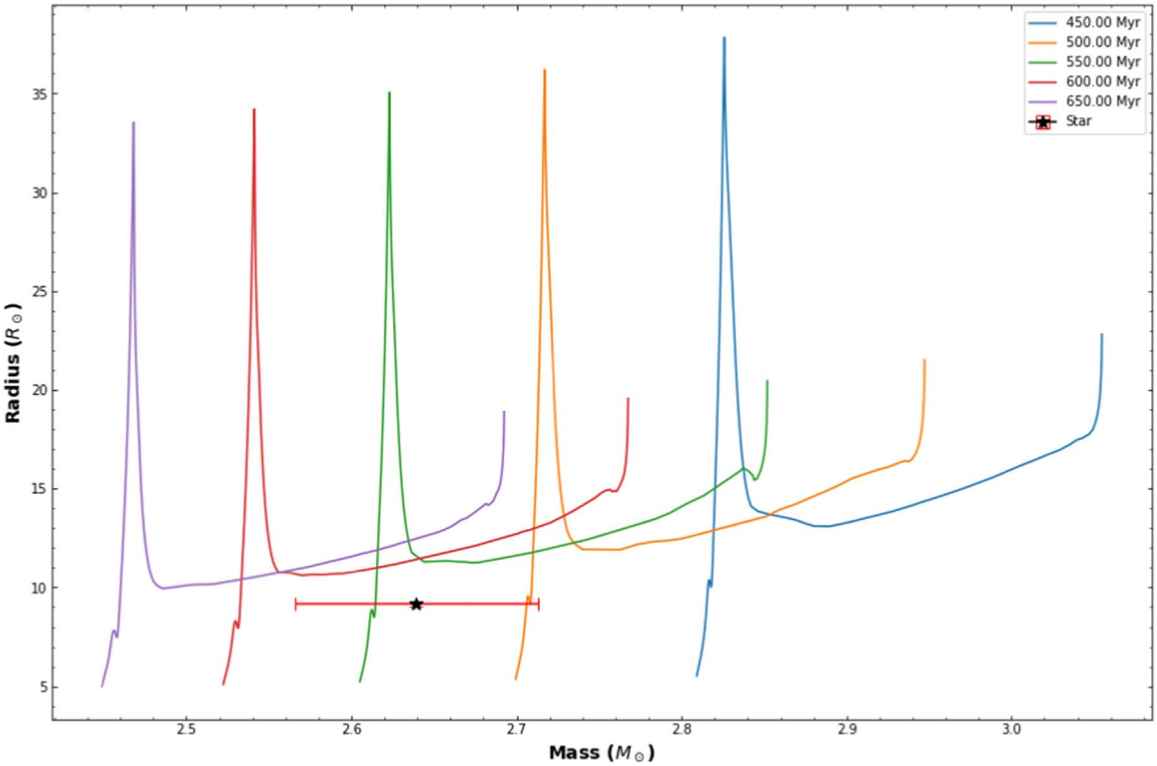

Figure 9. Mass–radius comparison of 12 Com A with MIST isochrones (Choi et al. 2016) showing only the subgiant and red giant branch phases.

Table 7
Fitted Parameters for 31 Com

mJD[a]	Visibility Normalization Factor	Angular Size (mas)
59656	1.125 ± 0.007	0.9195 ± 0.0017
59675	1.064 ± 0.005	0.9218 ± 0.0012
59677	1.104 ± 0.005	0.9274 ± 0.0011
59678	1.090 ± 0.003	0.9174 ± 0.0010

Note.
[a] mJD = HJD–2400000.

covered by spectroscopic abundance determinations for the cluster in the literature (see Section 1.2).

Literature values for the metallicity of Coma stars tend to vary by about ±0.08 dex. Utilizing different evolutionary tracks given this metallicity range results in an age difference of about ±14 Myr. Combining the uncertainties due to mass and metallicity in quadrature, we find that the age of the evolved star 12 Com A is constrained to 533±41 Myr.

4.3. Convective Core Overshooting

One of the major theoretical uncertainties in stellar evolution models is the treatment of convective core overshooting. Models from different groups utilize different overshoot lengths (parameterized in units of the pressure scale height), but they are generally assumed to ramp up from zero to a plateau value as a function of the stellar mass (Claret & Torres 2016). Stars with masses similar to those of the stars in 12 Com are assumed to have overshoot of the plateau value. We have used the PARSEC v1.2 and v2.0 isochrones to estimate the effects of uncertainties in convective core overshooting on the cluster age. Taking the overshoot in v1.2 to be approximately 0.25 the pressure scale heights (H_P) in v1.2 and approximately 0.2 the scale heights in v2.0 (Nguyen et al. 2022), we can see the effects on the luminosity of the subgiant branch that is inhabited by 12 Com A and 31 Com. PARSEC v1.2 and v2.0 isochrones differ by as much as 70 Myr for the CMD position of 12 Com A, but the $0.05H_P$ difference in convective core overshooting distances probably does not represent the uncertainty properly.

Claret & Torres (2016) semiempirically found from eclipsing binary stars that the overshoot length for stars with $M > 2M_\odot$ was $0.20H_P$, with an uncertainty of $0.03H_P$ for evolved stars (similar to 12 Com A). Taking this to be the best representation of the core overshooting uncertainty, we derive an associated systematic age uncertainty of 42 Myr.

4.4. White Dwarf Initial Final Mass Relation

An area of study that benefits immensely from an improved age is the white dwarf initial final mass relation (IFMR). Coma Ber is known to have a massive white dwarf member (WD 1216 + 260) with a measured "final" mass of $0.90 \pm 0.04M_\odot$ (Dobbie et al. 2009). A precise age can be used to derive the "initial" mass of the star before it became a white dwarf. Dobbie et al. (2009) used a cluster age of 500 ± 100 Myr to infer a progenitor star mass of $4.77^{+5.37}_{-0.97}M_\odot$. The large uncertainty is due primarily to uncertainty in the cluster age, as derived from the CMD analysis. As our understanding of the giant star mass loss prior to white dwarf emergence is poor, the precision measurement of a star's mass shortly before its major final mass loss is important (Kalirai et al. 2008).

With our new age measurement, we can greatly reduce the uncertainty in the initial mass. Using the Dobbie et al. cooling age $\tau_{\rm cool} = 363^{+46}_{-41}$ Myr and our new cluster age, we get an inferred progenitor star mass of $4.35^{+1.94}_{-0.73}M_\odot$, where the

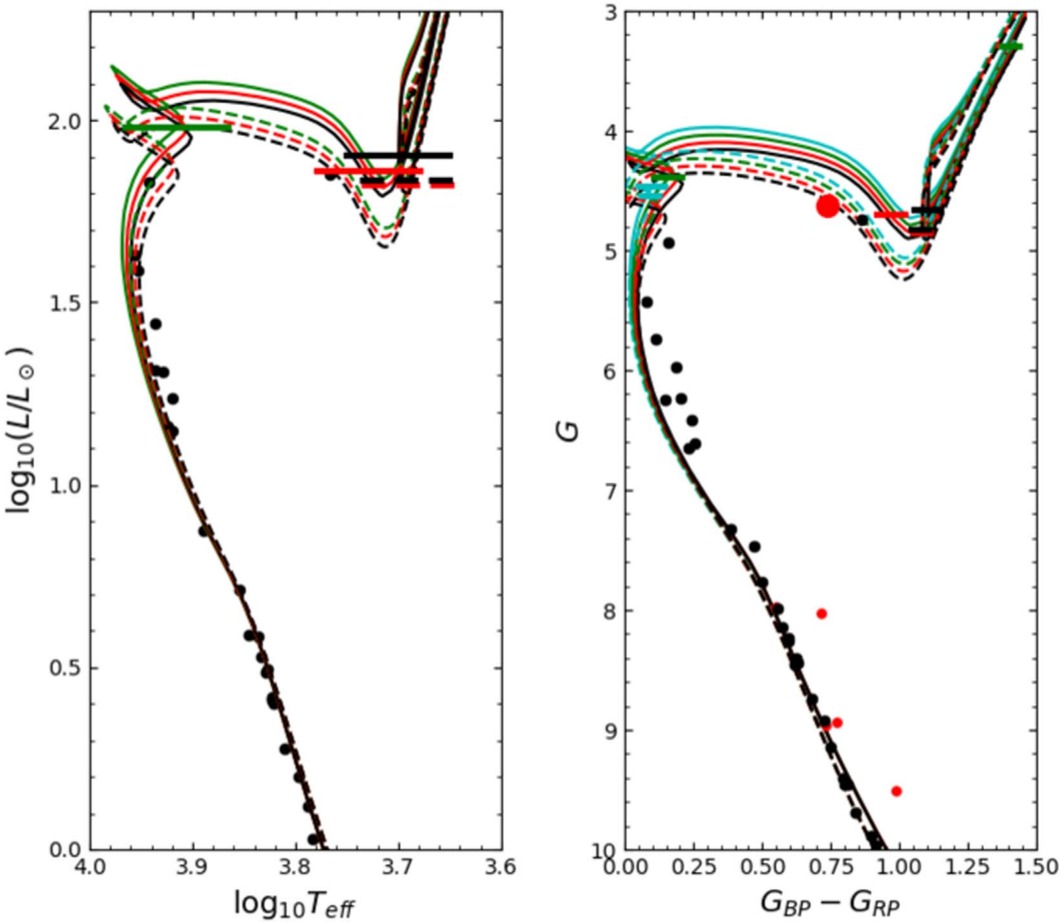

Figure 10. MIST (dashed lines; Choi et al. 2016) and PARSEC v1.2 (solid lines; Bressan et al. 2012) isochrones with $Z = 0.0152$ and $E(B-V) = 0$. The horizontal lines are the model positions of the primary star (assuming $2.64M_\odot$) in each isochrone. Left: HR diagram for Coma Ber stars. The isochrones have ages of 520 (green), 540 (red), and 560 (black) Myr. Right: Gaia color–magnitude diagram for Coma Ber stars. The isochrones have ages of 500–560 Myr in 20 Myr increments. The large topmost red point shows the combined light of 12 Com. Smaller red points show known binary systems.

uncertainty includes statistical and systematic (core overshooting) contributions. This cleanly rules out the possibility that the progenitor star had a mass near the white dwarf/neutron star production boundary. This gives us a much better picture of the progenitor star right before major mass loss.

5. Conclusions

Ages and masses are always useful in astronomy, and the age for an open cluster like Coma Ber can serve as a benchmark. Almost all age measurements for Coma Ber thus far have involved the analysis of color–magnitude diagrams (Tsvetkov 1989; Casewell et al. 2006; van Leeuwen 2009; Strassmeier et al. 2010; Singh et al. 2021), with significant uncertainties that result from a lack of constraints on some of the physics that affects the evolution of the stars. This paper marks the first look into the cluster age using an analysis of one of the most evolved stars in the cluster, thereby providing an important check on CMD analyses. Mass and age measurements for the evolved stars in 12 Com could not be made previously because the orbital inclination had not been determined. We take advantage of CHARA and PTI interferometric data to fit 12 Com's astrometric orbit and measure the masses of the primary and secondary stars: $2.64 \pm 0.07\ M_\odot$ and $2.10 \pm 0.03\ M_\odot$, respectively. Using the mass of the primary with MIST evolutionary tracks, we determine the cluster age using the photometry we derived for the primary and secondary stars. With our interferometric measurements, we were also able to resolve the primary star and measure the radius as $9.12 \pm 0.12R_\odot$. These results restrict the age of the cluster to $533 \pm 41 \pm 42$ Myr. Major contributions to the statistical uncertainty come from the mass uncertainty (due to a small number of secondary star radial velocities and large measurement uncertainties), and to a lesser extent, from metallicity uncertainty. We have also examined the effects of overshooting and how much it contributes to a systematic uncertainty in the age.

Reliably measured ages are necessary for other applications, such as honing the initial final mass relation for white dwarfs and determining the absolute calibration of the rotation period as an age indicator for isolated field main-sequence stars (Barnes 2003). Such gyrochronology studies generally use color as a stand-in for mass and have utilized standard isochrone fitting for ages. With significant improvements in precision for ages as well as reliable measurements for mass, the empirical models can be refined. The rotational properties of Coma Ber stars are not as well studied as for clusters like the Hyades, but ground-based measurements have been presented in Collier Cameron et al. (2009) and Terrien et al. (2014), and a combination of ground-based and TESS measurements were presented in Singh et al. (2021). Even without the absolute age calibration, gyrochronological studies are capable of relative

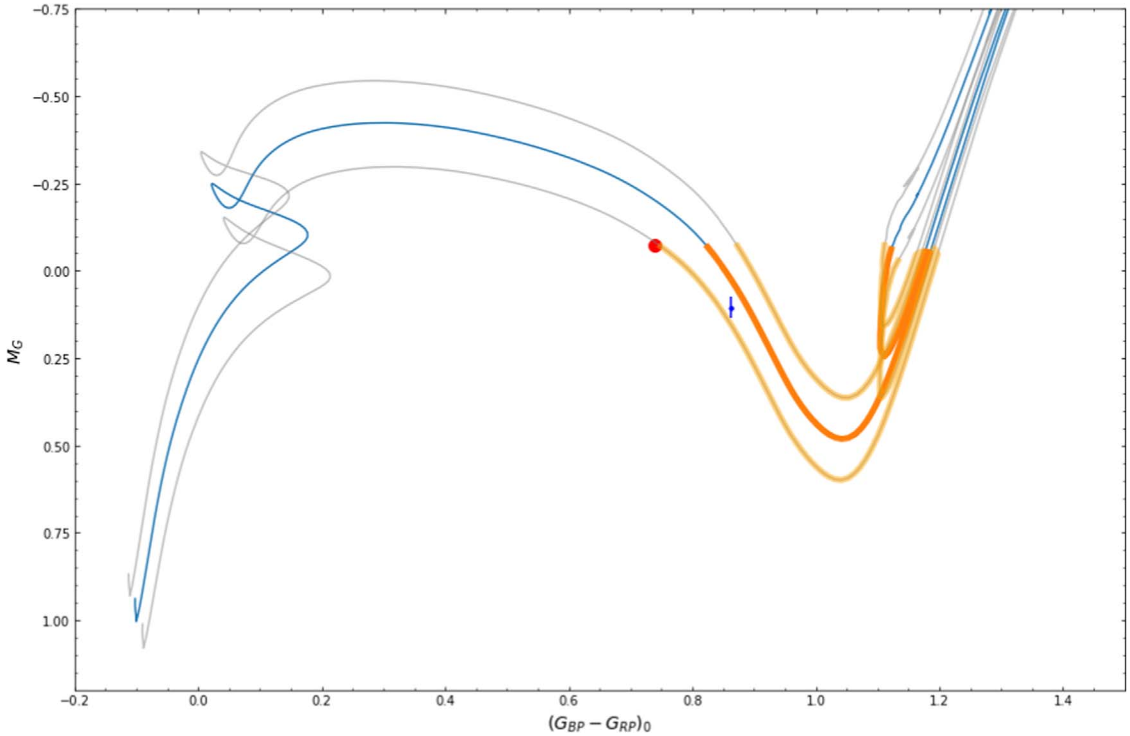

Figure 11. Evolutionary tracks (MESA) for a 2.64 $M_\odot$ star (blue curve) with [Fe/H] = 0.07. The combined photometry for 12 Com is shown with a red dot, using a distance of 87.0 ± 0.2 pc and reddening $E(B - V) = 0.00$ ($E(\mathrm{BP} - \mathrm{RP}) = 0.0022$). The photometric position of 31 Com is shown with a blue point. The dark orange curve shows the allowed regions for the giant to exist based on photometric considerations (ages 531–535 Myr for giant branch, 554–634 Myr for red clump). Evolution tracks for masses at $\pm 1\sigma$ ($\pm 0.07\ M_\odot$) are shown with gray/light orange curves.

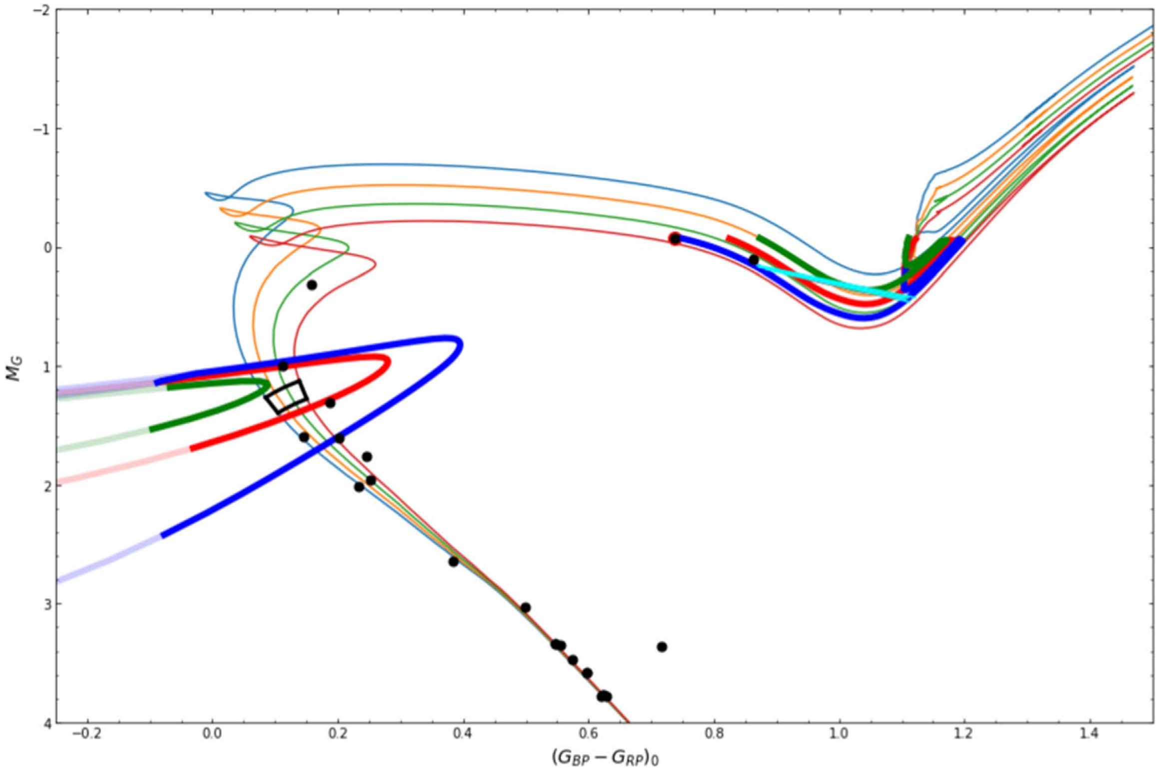

Figure 12. Gaia color–magnitude diagram for Coma Ber stars (black points), assuming reddening $E(B - V) = 0$ and distance modulus $(m - M)_0 = 4.67$. MIST isochrones (Choi et al. 2016) are shown for 450 Myr (blue) to 600 Myr (red) with 50 Myr spacing. Thick curves on the right show allowed portions of evolution tracks (fainter and redder than the binary) for the measured mass of 12 Com A as well as $\pm 1\sigma$ away in red, green, and blue, respectively. Corresponding positions for the secondary star (when 12 Com A's photometry is subtracted from that of the binary) are shown on the left. The cyan box shows the required position of 12 Com A if the secondary is in the isochrones between the thick blue lines. The black box encloses the predicted positions of the secondary in the isochrones, given its mass and $\pm 1\sigma$ uncertainties.

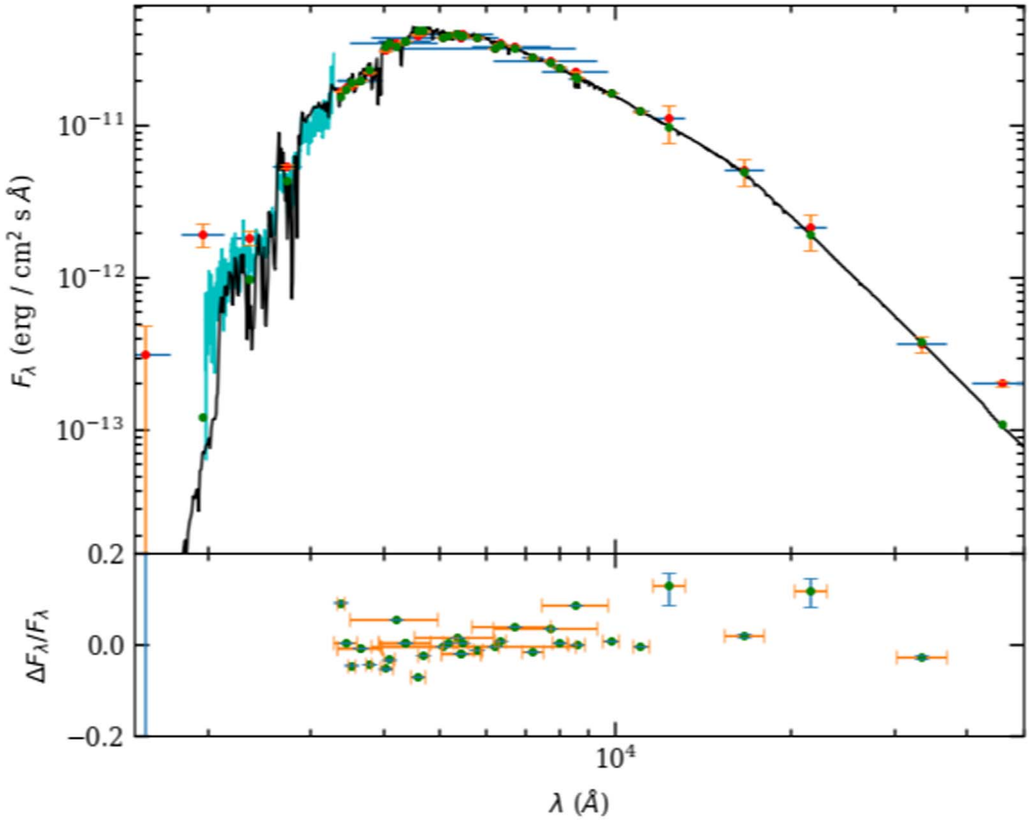

Figure 13. Top panel: spectral energy distribution of the single giant star 31 Com (orange points), with the photometric passbands for each point indicated with horizontal bars. The best-fit ATLAS9 model with $T_{\rm eff} = 5700$ K and $\log g = 3.5$ is shown in black, and the model predictions for each observed bandpass are shown with green points. A flux-calibrated IUE spectrum is shown in cyan. Bottom panel: relative flux residuals for each observed photometric bandpass.

age measurements, with Collier Cameron et al. finding that Coma was consistent with being the same age as the Hyades (Coma Ber 34 ± 41 Myr younger), and Singh et al. finding that Coma was coeval with the Hyades and Praesepe, despite differences in chemical composition between the clusters.

We gratefully acknowledge support from the National Science Foundation under grant AAG 1817217 to E.L.S. This research made use of observations from the SIMBAD database, operated at CDS, Strasbourg, France; and the WEBDA database, operated at the Institute for Astronomy of the University of Vienna.

This work is based upon observations obtained with the Georgia State University Center for High Angular Resolution Astronomy Array at Mount Wilson Observatory. The CHARA Array is supported by the National Science Foundation under grant No. AST-1636624 and AST-2034336. Institutional support has been provided from the GSU College of Arts and Sciences and the GSU Office of the Vice President for Research and Economic Development. Time at the CHARA Array was granted through the NOIRLab community access program (NOAO PropID: 2020A-0379; NOIRLab PropIDs: 2021A-0276, 2022A-118161; PI: E. Sandquist). MIRC-X received funding from the European Research Council (ERC) under the European Union's Horizon 2020 research and innovation program (Starting Grant "ImagePlanetFormDiscs" No. 639889). S.K. acknowledges support from ERC Consolidator Grant "GAIA-BIFROST" (grant No. 101003096) and STFC Consolidator Grand ST/V000721/1. J.D.M. acknowledges funding for the development of MIRC-X (NASA-XRP NNX16AD43G, NSF-AST 1909165) and MYSTIC (NSF-ATI 1506540, NSF-AST 1909165). The Palomar Testbed Interferometer was operated by the NASA Exoplanet Science Institute and the PTI collaboration. It was developed by the Jet Propulsion Laboratory, California Institute of Technology with funding provided from the National Aeronautics and Space Administration. This work has made use of services produced by the NASA Exoplanet Science Institute at the California Institute of Technology. This research has made use of the Jean-Marie Mariotti Center Aspro and SearchCal services.

Facilities: PO: PTI, CHARA (MIRC-X), OHP:1.93 m (ELODIE)

Software: BF-rvplotter (https://github.com/mrawls/BF-rvplotter).

Appendix
SEDs of 12 Com and 31 Com

We utilize a variety of sources for the SEDs of 31 Com. In the ultraviolet part of the spectrum, we obtained photometry from the Sky Survey Telescope on the TD-1 satellite (Thompson et al. 1978), which consisted of four passbands (centered at 1565 Å, 1965 Å, 2365 Å, and 2740 Å).

In the optical portion of the spectrum, we obtained the Strömgren *uvby* photometry from Paunzen (2015a). These magnitudes were then calibrated using reference fluxes from Gray (1998). We obtained photometry from the Johnson-13 color system as described in Johnson & Mitchell (1975) and the Tycho filters B_T and V_T from the Tycho Reference catalog (Høg et al. 2000). Both were calibrated using reference fluxes taken

Table 8
Photometry of 31 Com and 12 Com

			31 Com			12 Com		
Filter	$\lambda_{\rm eff}$ (Å) (Å)	m_λ	σ_m	F_λ (erg cm^{-2} s^{-1} Å^{-1})	m_λ	σ_m	F_λ (erg cm^{-2} s^{-1} Å^{-1})	Notes
$F1565$	1565	10.10	0.841	3.10×10^{-13}	6.61	0.048	7.68×10^{-12}	1
$F1965$	1965	8.11	0.186	1.93×10^{-12}	5.81	0.036	1.61×10^{-11}	1
$F2365$	2365	8.16	0.106	1.84×10^{-12}	6.10	0.034	1.22×10^{-11}	1
$F2740$	2740	7.00	0.022	5.38×10^{-12}	6.09	0.015	1.24×10^{-11}	1
$j33$	3374	5.74	0.010	1.68×10^{-11}	5.59	0.010	1.94×10^{-11}	2
u	3447	7.06	0.011	1.75×10^{-11}	6.89	0.007	2.05×10^{-11}	3
U_V	3450				7.35		2.15×10^{-11}	11
U_G	3471				6.08		2.13×10^{-11}	12
$m3500$	3500				6.61	0.016	2.07×10^{-11}	13
$j35$	3537	5.59	0.010	1.82×10^{-11}	5.51	0.010	1.97×10^{-11}	2
$u_{\rm SDSS}$	3551				6.47	0.060	2.31×10^{-11}	14
W_4	3554				5.51		2.20×10^{-11}	15
$m3571$	3571				6.59	0.016	2.04×10^{-11}	13
$m3636$	3636				6.43	0.016	2.27×10^{-11}	13
U	3663	5.81	0.004	1.98×10^{-11}	5.56	0.009	2.50×10^{-11}	7
U	3663	5.81		1.98×10^{-11}	5.57		2.47×10^{-11}	4
P_V	3740				6.69		3.02×10^{-11}	11
$j37$	3774	5.71	0.010	2.23×10^{-11}	5.56	0.010	2.58×10^{-11}	2
$B1_G$	4023				5.46		4.43×10^{-11}	12
$m4036$	4036				5.22	0.016	5.59×10^{-11}	13
$j40$	4046	5.89	0.010	3.12×10^{-11}	5.51	0.010	4.43×10^{-11}	2
X_V	4054				5.91		4.88×10^{-11}	11
v	4100	6.02	0.009	3.39×10^{-11}	5.62	0.005	4.91×10^{-11}	3
$m4167$	4167				5.22	0.016	5.26×10^{-11}	13
B_T	4220	5.72	0.014	3.49×10^{-11}	5.38	0.014	4.77×10^{-11}	5
B_G	4246				4.43		4.87×10^{-11}	12
$m4255$	4255				5.19	0.016	5.21×10^{-11}	13
B	4361	5.61	0.005	3.60×10^{-11}	5.29	0.005	4.82×10^{-11}	7
B	4361	5.61		3.60×10^{-11}	5.30		4.79×10^{-11}	4
B_4	4382				5.30		5.03×10^{-11}	15
$m4400$	4400				5.12	0.016	5.20×10^{-11}	13
$B2_G$	4482				5.78		5.27×10^{-11}	12
$m4565$	4565				5.01	0.016	5.31×10^{-11}	13
$j45$	4586	5.46	0.010	3.92×10^{-11}	5.18	0.010	5.08×10^{-11}	2
Y_V	4665				5.24		5.44×10^{-11}	11
$g_{\rm SDSS}$	4686				4.98	0.030	5.04×10^{-11}	14
b	4688	5.38	0.019	4.15×10^{-11}	5.12	0.004	5.30×10^{-11}	3
$m4785$	4785				4.96	0.016	5.09×10^{-11}	13
$m5000$	5000				4.93	0.016	4.77×10^{-11}	13
$G_{\rm BP}$	5051	5.09	0.003	3.80×10^{-11}	4.92	0.003	4.45×10^{-11}	6
Z_V	5162				4.95		4.80×10^{-11}	11
$j52$	5180	5.09	0.010	3.90×10^{-11}	4.94	0.010	4.49×10^{-11}	2
$m5263$	5263				4.88	0.016	4.52×10^{-11}	13
V_T	5350	5.00	0.009	4.03×10^{-11}	4.86	0.009	4.59×10^{-11}	5
$V1_G$	5402				5.53		4.58×10^{-11}	12
V_V	5442				4.76		4.71×10^{-11}	11
V	5448	4.94	0.007	3.84×10^{-11}	4.80	0.018	4.35×10^{-11}	7
V	5448	4.94		3.84×10^{-11}	4.81		4.32×10^{-11}	4
y	5480	4.94	0.026	3.95×10^{-11}	4.79	0.006	4.51×10^{-11}	3
V_G	5504				4.78	0.028	4.56×10^{-11}	12
V_4	5519				4.80		4.50×10^{-11}	15
$j58$	5806	4.76	0.010	3.79×10^{-11}	4.67	0.010	4.09×10^{-11}	2
G_G	5814				5.86		4.31×10^{-11}	12
$m5840$	5840				4.76	0.016	4.11×10^{-11}	13
$r_{\rm SDSS}$	6166				4.70	0.030	3.77×10^{-11}	14
G	6230	4.74	0.003	3.24×10^{-11}	4.62	0.003	3.59×10^{-11}	6
$m6300$	6300				4.72	0.016	3.65×10^{-11}	13
$j63$	6349	4.55	0.010	3.45×10^{-11}	4.49	0.010	3.66×10^{-11}	2
S_V	6534				4.28		3.62×10^{-11}	11
R_J	6695	4.39		3.30×10^{-11}	4.34		3.46×10^{-11}	7
$m6710$	6710				4.68	0.016	3.34×10^{-11}	13
$m7100$	7100				4.66	0.016	3.03×10^{-11}	13

Table 8
(Continued)

Filter	$\lambda_{\rm eff}$ (Å) (Å)	31 Com			12 Com			Notes
		m_λ	σ_m	F_λ (erg cm^{-2} s^{-1} Å^{-1})	m_λ	σ_m	F_λ (erg cm^{-2} s^{-1} Å^{-1})	
R_4	7166				4.34		3.11×10^{-11}	15
$j72$	7222	4.37	0.010	2.79×10^{-11}	4.33	0.010	2.87×10^{-11}	2
$m7400$	7400				4.60	0.016	2.95×10^{-11}	13
$G_{\rm RP}$	7726	4.23	0.005	2.67×10^{-11}	4.18	0.004	2.79×10^{-11}	6
$j80$	7993	4.18	0.010	2.40×10^{-11}	4.17	0.010	2.42×10^{-11}	2
I_J	8565	4.04		2.26×10^{-11}	4.01		2.32×10^{-11}	7
$j86$	8577	4.12	0.010	2.05×10^{-11}	4.11	0.010	2.07×10^{-11}	2
$j99$	9813	4.04	0.010	1.64×10^{-11}	4.00	0.010	1.69×10^{-11}	2
$j110$	11037	3.91	0.010	1.24×10^{-11}	3.88	0.010	1.28×10^{-11}	2
J	12350	3.63	0.292	1.11×10^{-11}	3.78	0.254	9.62×10^{-12}	8
H	16620	3.37	0.218	5.10×10^{-12}	3.40	0.216	4.94×10^{-12}	8
K_S	21590	3.26	0.286	2.13×10^{-12}	3.24	0.244	2.17×10^{-12}	8
$W1$	33526	3.37	0.132	3.66×10^{-13}	3.20	0.076	4.29×10^{-13}	9
$W2$	46028	2.70	0.053	2.01×10^{-13}	2.47	0.071	2.49×10^{-13}	9
$S9W$	82283	3.11	0.004	1.20×10^{-14}	2.95	0.011	1.39×10^{-14}	10
$W3$	115608	3.34	0.014	3.00×10^{-15}	3.08	0.010	3.81×10^{-15}	9
$L18W$	176094	3.08	0.042	6.06×10^{-16}	2.87	0.070	7.40×10^{-16}	10
$W4$	220883	3.24	0.021	2.58×10^{-16}	3.11	0.018	2.91×10^{-16}	9

Note. 1. Gondhalekar et al. (1980), 2. Johnson & Mitchell (1975), 3. Paunzen (2015), 4. Morel & Magnenat (1978), 5. Høg et al. (2000), 6. Gaia Collaboration et al. (2021), 7. Flynn & Mermilliod (1991), 8. Skrutskie et al. (2006), 9. Wright et al. (2010), 10. Murakami et al. (2007), 11. Dzěrvitis & Paupers (1990), 12. Rufener (1988), 13. Clampitt & Burstein (1997), 14. Blanton et al. (2017), 15. Kornilov et al. (1991).

(This table is available in machine-readable form.)

from the Spanish Virtual Observatory (SVO) Filter Profile Service (Rodrigo et al. 2012). We also obtained photometry in the Johnson–Cousins filters (Morel & Magnenat 1978), which were calibrated to flux using Table A2 of Bessell et al. (1998). Four photometric measurements in the WBVR 4-color system were taken by Kornilov et al. (1991) and calibrated with zero-points from Mann & von Braun (2015). Finally, we used the high-precision Gaia data in the G, $G_{\rm BP}$, and $G_{\rm RP}$ bandpasses from Early Data Release 3 (Gaia Collaboration et al. 2021).

For the infrared part of the spectrum, we utilized photometry in the JHK_s bands from the Two-Micron All-Sky Survey (2MASS; Skrutskie et al. 2006). We utilized the reference fluxes from Claret & Torres (2016) to convert to fluxes. Photometry from four bands (W1, W2, W3, and W4) in the Wide Field Infrared Survey Explorer (WISE; Wright et al. 2010) were taken and converted using their own reference fluxes. Finally, in the infrared range, we obtained fluxes from the AKARI satellite infrared camera all-sky survey in the $S9W$ and $L18W$ filters (Murakami et al. 2007).

A comprehensive list of all the photometric measurements used is shown in Table 8. All the above photometric sources are also utilized for 12 Com. However, 12 Com has a few additional sources, mostly in the optical. In particular, we obtained observations from the Geneva Observatory (Rufener 1988), the seven-filter Vilnius photometry (Dzěrvitis & Paupers 1990), spectrophotometric measurements from Clampitt & Burstein (1997), and the Sloan Digital Sky Survey (SDSS; Blanton et al. 2017).

To get properties of 31 Com, we fit the photometric SED using ATLAS9 (Castelli & Kurucz 2003) models with [Fe/H] = 0.0 and $\log g = 3.5$. This model fit is shown in Figure 13. This resulted in an effective temperature of approximately 5700 K and a bolometric flux $F_{\rm bol} = 2.86 \times 10^{-7}$ erg cm^{-2} s^{-1}. We estimate statistical uncertainties of ±40 K in $T_{\rm eff}$ from scatter in infrared-flux method temperatures from the J, H, and K_s bands, and of $\pm 3 \times 10^{-9}$ erg cm^{-2} s^{-1} in $F_{\rm bol}$ using fits with different $T_{\rm eff}$ within the range. Metallicity uncertainties contribute negligibly in these fits. 31 Com is known to be magnetically active and an X-ray and UV emitter, so we do not worry greatly about the disagreement between photometric observations and models for $\lambda < 3000$ Å. An International Ultraviolet Explorer (IUE) spectrum of the star (data I.D.: LWR04860; P.I.: R. F. Garrison) shows approximate agreement with the fitted model through the ultraviolet. Pairing the bolometric flux with a distance of 86.99 pc corresponds to a luminosity $L = 63.6 \pm 1.0\, L_\odot$, typical of red giant branch stars. This luminosity then corresponds to a radius of $8.18 \pm 0.13\, R_\odot$. This agrees very well with the radius derived from interferometry of $8.36 \pm 0.15\, R_\odot$.

ORCID iDs

Eric L. Sandquist https://orcid.org/0000-0003-4070-4881
Gail H. Schaefer https://orcid.org/0000-0001-5415-9189
Christopher D. Farrington https://orcid.org/0000-0001-9939-2830
John D. Monnier https://orcid.org/0000-0002-3380-3307
Narsireddy Anugu https://orcid.org/0000-0002-2208-6541
Cyprien Lanthermann https://orcid.org/0000-0001-9745-5834
Robert Klement https://orcid.org/0000-0002-4313-0169
Jacob Ennis https://orcid.org/0000-0002-1575-4310
Benjamin R. Setterholm https://orcid.org/0000-0001-5980-0246
Tyler Gardner https://orcid.org/0000-0002-3003-3183
Stefan Kraus https://orcid.org/0000-0001-6017-8773
Claire L. Davies https://orcid.org/0000-0001-9764-2357
Jerome A. Orosz https://orcid.org/0000-0001-9647-2886

References

Abt, H. A., & Willmarth, D. W. 1999, ApJ, 521, 682
Anugu, N., Le Bouquin, J.-B., Monnier, J. D., et al. 2020, AJ, 160, 158
Asplund, M., Grevesse, N., Sauval, A. J., & Scott, P. 2009, ARA&A, 47, 481
Avni, Y. 1976, ApJ, 210, 642
Bailer-Jones, C. A. L., Rybizki, J., Fouesneau, M., Demleitner, M., & Andrae, R. 2021, AJ, 161, 147
Baraffe, I., Chabrier, G., Allard, F., & Hauschildt, P. H. 1998, A&A, 337, 403
Barnes, S. A. 2003, ApJ, 586, 464
Beavers, W. I., & Eitter, J. J. 1986, ApJS, 62, 147
Bessell, M. S., Castelli, F., & Plez, B. 1998, A&A, 333, 231
Blanton, M. R., Bershady, M. A., Abolfathi, B., et al. 2017, AJ, 154, 28
Bourges, L., Mella, G., Lafrasse, S., et al. 2017, yCat, II/346
Brandt, T. D., & Huang, C. X. 2015, ApJ, 807, 24
Bressan, A., Marigo, P., Girardi, L., et al. 2012, MNRAS, 427, 127
Cannon, J. B. 1920, PDAO, 4, 253
Casewell, S. L., Jameson, R. F., & Dobbie, P. D. 2006, MNRAS, 365, 447
Castelli, F., & Kurucz, R. L. 2003, in IAU Symp. 210, Modelling of Stellar Atmospheres, ed. N. Piskunov, W. W. Weiss, & D. F. Gray (San Francisco, CA: ASP), A20
Charbonneau, P. 1995, ApJS, 101, 309
Choi, J., Dotter, A., Conroy, C., et al. 2016, ApJ, 823, 102
Clampitt, L., & Burstein, D. 1997, AJ, 114, 699
Claret, A., & Torres, G. 2016, A&A, 592, A15
Colavita, M. M., Wallace, J. K., Hines, B. E., et al. 1999, ApJ, 510, 505
Collier Cameron, A., Davidson, V. A., Hebb, L., et al. 2009, MNRAS, 400, 451
Dobbie, P. D., Casewell, S. L., Burleigh, M. R., & Boyce, D. D. 2009, MNRAS, 395, 1591
Dzěrvitis, U., & Paupers, O. 1990, ISKZ, 33, 58
Flynn, C., & Mermilliod, J. C. 1991, A&A, 250, 400
Friel, E. D., & Boesgaard, A. M. 1992, ApJ, 387, 170
Fürnkranz, V., Meingast, S., & Alves, J. 2019, A&A, 624, L11
Gardner, T., Monnier, J. D., Fekel, F. C., et al. 2022, AJ, 164, 184
Gebran, M., Monier, R., & Richard, O. 2008, A&A, 479, 189
Glushkova, E. V., & Rastorguev, A. S. 1991, SvA Letters, 17, 13
Gondhalekar, P. M., Phillips, A. P., & Wilson, R. 1980, A&A, 85, 272
González, J. F., & Levato, H. 2006, A&A, 448, 283
Gray, R. O. 1998, AJ, 116, 482
Griffin, R. E. M., & Griffin, R. F. 2011, AN, 332, 105
Griffin, R. F. 1969, MNRAS, 145, 163
Gaia Collaboration, Brown, A. G. A., Vallenari, A., et al. 2018, A&A, 616, A1
Gaia Collaboration, Smart, R. L., Sarro, L. M., et al. 2021, A&A, 649, A6
Harper, W. E. 1934, PDAO, 6, 149
Herbig, G. H., & Turner, B. A. 1953, ApJ, 118, 477
Høg, E., Fabricius, C., Makarov, V. V., et al. 2000, A&A, 355, L27
Holmberg, J., Nordström, B., & Andersen, J. 2007, A&A, 475, 519
Johnson, H. L., & Mitchell, R. I. 1975, RMxAA, 1, 299
Kalirai, J. S., Hansen, B. M. S., Kelson, D. D., et al. 2008, ApJ, 676, 594
Keenan, P. C., & McNeil, R. C. 1989, ApJS, 71, 245
Kornilov, V. G., Volkov, I. M., Zakharov, A. I., et al. 1991, TrSht, 63, 1
Magg, E., Bergemann, M., Serenelli, A., et al. 2022, A&A, 661, A140
Mann, A. W., & von Braun, K. 2015, PASP, 127, 102
Massarotti, A., Latham, D. W., Stefanik, R. P., & Fogel, J. 2008, AJ, 135, 209
Mermilliod, J. C., Grenon, M., & Mayor, M. 2008, A&A, 491, 951
Monnier, J. D. 2007, NewAR, 51, 604
Morel, M., & Magnenat, P. 1978, A&AS, 34, 477
Moultaka, J., Ilovaisky, S. A., Prugniel, P., & Soubiran, C. 2004, PASP, 116, 693
Murakami, H., Baba, H., Barthel, P., et al. 2007, PASJ, 59, S369
Nguyen, C. T., Costa, G., Girardi, L., et al. 2022, A&A, 665, A126
Orosz, J. A., & Hauschildt, P. H. 2000, A&A, 364, 265
Palacios, A., Gebran, M., Josselin, E., et al. 2010, A&A, 516, A13
Parsons, S. B. 1983, ApJS, 53, 553
Paunzen, E. 2015, A&A, 580, A23
Perraut, K., Cunha, M., Romanovskaya, A., et al. 2020, A&A, 642, A101
Rodrigo, C., Solano, E., & Bayo, A. 2012, SVO Filter Profile Service Version 1.0, IVOA, doi:10.5479/ADS/bib/2012ivoa.rept.1015R
Rucinski, S. M. 1992, AJ, 104, 1968
Rufener, F. 1988, A&AS, 78, 469
Schaefer, G. H., Hummel, C. A., Gies, D. R., et al. 2016, AJ, 152, 213
Singh, K., Rothstein, P., Curtis, J. L., Núñez, A., & Agüeros, M. A. 2021, RNAAS, 5, 84
Skrutskie, M. F., Cutri, R. M., Stiening, R., et al. 2006, AJ, 131, 1163
Souto, D., Cunha, K., & Smith, V. 2021, ApJ, 917, 11
Strassmeier, K. G., Granzer, T., Kopf, M., et al. 2010, A&A, 520, A52
Strassmeier, K. G., Washuttl, A., & Rice, J. B. 1994, IBVS, 3994, 1
Tang, S.-Y., Pang, X., Yuan, Z., et al. 2019, ApJ, 877, 12
Taylor, B. J. 2006, AJ, 132, 2453
ten Brummelaar, T. A., McAlister, H. A., Ridgway, S. T., et al. 2005, ApJ, 628, 453
Terrien, R. C., Mahadevan, S., Deshpande, R., et al. 2014, ApJ, 782, 61
Thompson, G. I., Nandy, K., Jamar, C., et al. 1978, Catalogue of Stellar Ultraviolet Fluxes: a Compilation of Absolute Stellar Fluxes Measured by the Sky Survey Telescope (S2/68) Aboard the ESRO Satellite TD-1/ (Swindon: Science Research Council)
Tsvetkov, T. G. 1989, Ap&SS, 151, 47
van Leeuwen, F. 2009, A&A, 497, 209
Vinter Hansen, J. M. 1940, PASP, 52, 399
Wright, E. L., Eisenhardt, P. R. M., Mainzer, A. K., et al. 2010, AJ, 140, 1868